

Vista Research Technical Report No. 2096 TM-98-001

**Robust Analysis of Aerothermal Data**

Prepared by:

G. Papanicolaou and K. Solna  
Department of Mathematics  
Stanford University, Stanford CA 94305

C. Rino and V. Kruger  
Vista Research Inc.

Prepared For:

Airforce Office of Scientific Research  
110 Duncan Avenue room B115  
Bolling AFB DC 20332-8080

Contract No. F49620-97-C-0018

Attention: Dr. Arje Nachmann

17 February 1998



**VISTA RESEARCH, INC.**

100 View Street • P.O. Box 998  
Mountain View, CA 94042 • (415) 966-1171

## REPORT DOCUMENTATION PAGE

Form Approved

Public reporting burden for this collection of information is estimated to average 1 hour per response, including the time for reviewing instructions, the collection of information. Send comments regarding this burden estimate or any other aspect of this collection of information, including Operations and Reports, 1215 Jefferson Davis Highway, Suite 1204, Arlington, VA 22202-4302, and to the Office of Management and Budget,

AFRL-SR-BL-TR-98-

and reviewing  
information

1. AGENCY USE ONLY (Leave blank)

2. REPORT DATE

17 Feb 98

3. REI

0271

17

4. TITLE AND SUBTITLE

ROBUST ANALYSIS OF AEROTHERMAL DATA

5. FUNDING NUMBERS

F49620-97-C-0018

6. AUTHOR(S)

Professors G. Papanicolaou and K. Solna

7. PERFORMING ORGANIZATION NAME(S) AND ADDRESS(ES)

VISTA RESEARCH, Inc.  
100 View Street, PO Box 998  
Mountain View, CA 94042

8. PERFORMING ORGANIZATION  
REPORT NUMBER

9. SPONSORING/MONITORING AGENCY NAME(S) AND ADDRESS(ES)

AFOSR/NM  
110 Duncan Avenue Room B115  
Bolling AFB DC 20332-8050

10. SPONSORING/MONITORING  
AGENCY REPORT NUMBER

11. SUPPLEMENTARY NOTES

12a. DISTRIBUTION AVAILABILITY STATEMENT

Approved for public release; distribution unlimited.

19980331 028

13. ABSTRACT (Maximum 200 words)

The main premise driving our analysis of temperature data from a turbulent atmosphere is that it is a local power law process. This means that the power law itself-the power (slope) and the multiplicative constant (log intercept)-is not a constant but a slowly varying function, deterministic or random. We estimate the slope and log intercept of the scale spectrum by appropriately segmenting the data and then removing segmentation effects by a filtering process. An important aspect of the model that we use is separation of scales in the variation of the estimate parameters (slope and log intercept) from the underlying process that generates the power law spectra. This will be the starting point for a detailed theoretical development of the methods that we have introduced here.

14. SUBJECT TERMS

Keywords: atmospheric turbulence, signal-processing

15. NUMBER OF PAGES

16. PRICE CODE

17. SECURITY CLASSIFICATION  
OF REPORT

Unclassified

18. SECURITY CLASSIFICATION  
OF THIS PAGE

Unclassified

19. SECURITY CLASSIFICATION  
OF ABSTRACT

Unclassified

20. LIMITATION OF  
ABSTRACT

UL

# Contents

<b>1 Preliminary Analysis</b>	<b>1</b>
1.1 Introduction . . . . .	1
1.2 Data Processing . . . . .	2
1.2.1 Data Extraction . . . . .	2
1.2.2 Parameter estimation . . . . .	2
1.2.3 Scale spectra versus conventional spectra . . . . .	4
1.3 Analysis of file 95135-04 data . . . . .	10
1.3.1 Analysis by data sub-segment . . . . .	10
1.3.2 Variability of power-law parameters from fixed wave number ranges . . . . .	16
1.4 Analysis of Bahrain Data . . . . .	19
1.5 Summary . . . . .	23
<b>2 Scale spectral analysis</b>	<b>25</b>
2.1 The data . . . . .	25
2.2 The wavelet analysis . . . . .	28
2.3 Filtering of the parameter processes . . . . .	31
2.3.1 Synthetic data . . . . .	31
2.3.2 Measured data . . . . .	33
2.3.3 Filtering of the slope and log intercept processes . . . . .	34
2.4 Simulated data based on the filtered slope and log intercept processes . . . . .	36
2.4.1 Replication with filtered slope and log intercept . . . . .	36
2.4.2 Sampling error . . . . .	38
2.4.3 Error in parametric fitting of scale spectrum . . . . .	47
2.4.4 Replication with random slope and log intercept . . . . .	50
2.4.5 Intrinsic variability of the slope and log intercept process . . . . .	51
2.5 Summary and conclusions . . . . .	52
<b>A Simulation of power law processes</b>	<b>57</b>
A.1 Model of the process . . . . .	57
A.2 Direct simulation of a stationary sequence . . . . .	58
A.3 Sequential simulation of a stationary sequence . . . . .	58
A.4 Screening simulation in non-stationary case. . . . .	60
<b>B Analysis of other aerothermal data sets</b>	<b>61</b>
B.1 The 03 data set . . . . .	62
B.2 The 15 data set . . . . .	66

# 1 Preliminary Analysis

## 1.1 Introduction

The earth's atmosphere can affect the propagation of laser beams significantly. Large-scale structure alters the beam trajectory, while the cumulative effect of small-scale structure induced by atmospheric turbulence imparts a random modulation that can defocus the beam. These phenomena are accommodated in propagation models by partitioning the refractive index field as

$$n(\mathbf{r}, t) = \bar{n}(\mathbf{r}, t) + \delta n(\mathbf{r}, t), \quad (1.1)$$

where  $\bar{n}(\mathbf{r}, t)$  represents the background and  $\delta n(\mathbf{r}, t)$  represents small-scale structure. The partitioning is somewhat arbitrary, but  $\delta n(\mathbf{r}, t)$  can be constructed formally by high-pass-filtering  $n(\mathbf{r}, t)$  on the spatial variable. The performance of the optical system in the Airborne Laser Extended Atmospheric Characterization Experiment (ABLE ACE) is not affected by structure larger than a few kilometers; moreover, the temperature probe that measures the turbulent structure scans rapidly enough that variations within typical analysis segments can be ignored. Thus, high-pass filtering the output of the temperature probe prior to digitization effectively extracts the fluctuating component. The filtered temperature fluctuations determine the refractive index fluctuation,  $\delta n(\mathbf{r}, t)$ , via the relation

$$\delta n = -\frac{79 \times 10^{-6} p}{T^2} \delta T. \quad (1.2)$$

Temperature, formally a passive scalar, fluctuates in response to the velocity turbulence. If the turbulence has achieved a sustained homogeneous and isotropic state, the power spectral density (PSD) of the temperature fluctuations admits an inertial subrange with a 5/3 power-law spectral index. In a real environment, however, the probe encounters turbulent structure in various states of evolution and decay. Thus, the ideal model applies only to disjoint data segments, potentially of varying length. As a consequence, any attempt to measure parameters that characterize the turbulence will fluctuate in response to sampling errors as well as in response to processes intrinsic to the structure evolution. Careful consideration must be given to data segmentation, parameter estimation, and the analysis of the parameter fluctuations to properly reconstruct the turbulence for modeling purposes.

This report demonstrates new analysis procedures that treat the standard power-law parameters as random processes that have a richer structure than mean values corrupted by sample noise. Ultimately, the intrinsic structure of the parameter processes may provide new insight into the physics of the evolving turbulence. In the near term, the analysis is important for determining the structure and deployment of phase screens used to emulate the effects of the refractive index structure in simulations of the ABLE ACE optical processor.

Spectral analysis has played a seminal role in the theory and measurement of turbulence, although the guidelines for standard spectral analyses methods are derived from statistically homogeneous or locally homogeneous models. Within the context of these procedures, a fixed sample rate determines the smallest spatial structure that can be resolved ( $\Delta x = V \Delta t$ ), but there is considerable flexibility in choosing the data segmentation and subsequent parameter extraction operations. In particular, data segmentation determines the minimum scale at which the parameters that characterize the turbulence can vary. Thus, it is important to develop procedures that cleanly separate intrinsic structure in the extracted parameters from sample noise. The research described in this report addresses this problem within the context of the ABLE ACE objectives.

In Part I we describe the procedures that have been developed to isolate a power-law subrange in the temperature fluctuation data. These procedures are reviewed within the context of standard



parameter estimation procedures that have been applied to the ABLE ACE data. This is important because the power-law range of spectral wave numbers that represent scale-invariant turbulence varies with the strength of turbulence. While this suggests using a variable window, it is desirable to fix the wavelength range over which turbulence parameters are extracted. The low-frequency limit is determined by the block length for analysis as described below. The upper limit ideally would be determined by diffusion processes. Vagaries of the data further restrict the spectral regime where viable parameter estimates can be made. The analysis presented in Part I highlights the variability of the the power-law slope and strength parameters that ultimately determine system performance. In Part 2 these parameter variations are subjected to an in-depth statistical analysis that provides a new framework for interpreting the turbulence parameters.

## 1.2 Data Processing

### 1.2.1 Data Extraction

The preliminary processing of the aero-thermal probe data follows the procedures specified in the ABLE ACE report PL-TR-96-1084, Part 1, Chapter 6. The raw data have been calibrated to represent temperature fluctuation in degrees Celsius. Although the specifics of the mission (date, location, altitude, airspeed, etc.) are not contained in all the data files made available to us, the approximate values summarized in Table 1.1 have been used to convert temperature fluctuations to refraction index fluctuations via (1.2) when the actual values were not known. The Nyquist frequency corresponding to the 2-cm sample separation is  $K_N = \pi/\Delta x = 157$  rad/m. Following the ABLE ACE terminology, a block of length  $L_B$  containing  $N_B = L_B/\Delta x$  samples is the smallest segment to which spectral analysis is applied. Block sizes are constrained so that  $N_B = 2^M$ . Data segments are generated by averaging the results from several blocks. The block length determines the finest level of segmentation and, thereby, the largest spatial scale that can be resolved, while the segment length determines the smallest scale over which parameter estimates can vary.

In building data segments, overlap (blocks common to more than one segment) is avoided because it introduces correlation in the fluctuation of the estimated parameters that complicates their interpretation, as described in Part 2. For the same reason, it is desirable to estimate parameters prior to any averaging operations that are not intrinsic to the spectral estimation procedures. Because of the fluctuation statistics of standard PSD estimates and the nonlinear logarithm operation that is applied prior to least-squares extraction of the turbulence parameters, however, some compromises are necessary. We show, nonetheless, that wavelet scale spectra are less prone to such bias.

Table 1.1: Parameter Values

Parameter	Value	Comment
Altitude	40,000 ft	From Table 6-1
Temperature	210° K	From Table 6-1
Pressure	200 mb	From Standard Atmosphere
Sample separation	2 cm	$\Leftarrow 12$ kHz @ 210 m/s

### 1.2.2 Parameter estimation

Turbulence is characterized mainly by the inertial subrange where the spectral density function varies as  $CK^{-\eta}$ . Our objective is to obtain stable unbiased estimates of  $C$  and  $\eta$ , which we interpret

as random processes in their own right. A standard approach applies a linear least-squares fit to  $\log(\tilde{\Phi}(K_n))$ , where  $\tilde{\Phi}(K_n)$  is an estimate of the PSD at spatial wave number  $n\Delta K$ . There are a number of potential problems with this approach. The location of the inertial subrange is unknown a priori; moreover, the logarithm of the spectral estimate has complicated fluctuation statistics that can introduce biases in their own right. To provide an objective criterion for locating power-law segments, the least-squares fit has been determined over spectral windows starting at the lowest non-zero frequency and continuing to successively higher frequencies until the Nyquist frequency is encountered at the upper end of the fitting interval. A uniform power-law segment should yield, on average, the same fit parameters irrespective of the fit range. Beyond that, we rely on simulations to verify that the sampling noise introduced by the parameter extraction process is being isolated and removed.

Standard processing starts with an estimate of the spectral density function (PSD). The unnormalized discrete Fourier transform (DFT) evaluated by most FFT algorithms is defined as

$$\hat{X}_n = \sum_{k=0}^{N_B-1} X_k \exp\{-2\pi i n k / N_B\}. \quad (1.3)$$

The following relation between the sample second moment of the process and the total spectral intensity can be verified by direct computation:

$$\frac{1}{N_B} \sum_{k=0}^{N_B-1} X_k^2 = \sum_{n=0}^{N_B-1} |\hat{X}_n|^2 / N_B^2, \quad (1.4)$$

Thus, the “raw” periodogram,

$$PSD_n \equiv |\hat{X}_n|^2 / N_B^2, \quad (1.5)$$

is the most basic PSD estimator. For the class of real processes of interest here, the PSD is symmetric. It follows that the Parseval relation that equates the sample second moment to the total PSD intensity can be written as

$$\frac{1}{N_B} \sum_{k=0}^{N_B-1} X_k^2 = PSD_0 + 2 \sum_{n=1}^{N_B/2-1} PSD_n + PSD_{N_B/2}. \quad (1.6)$$

It is well known that the raw periodogram has fluctuation statistics that do not converge with increasing block size. To circumvent this problem, one uses a combination of weighting functions and block averages. It is sufficient for our immediate purposes simply to note that the weighting function is normalized to minimize the bias introduced by the spectral smoothing that results from applying the weighting function. Other operations such as mean removal, detrending, and zero padding further complicate the interpretation of the parameter fluctuations. Thus, we have not employed any techniques beyond applying standard window functions and block averaging.

For ABLE ACE it is also important to maintain absolute scales. Upon extracting a parametric representation of the form  $\Phi(K_n) \sim CK_n^{-\eta}$ , it is desirable to present  $C$  in units such that a statistically equivalent realization of the process will reproduce the structure sensed by a light beam traversing the same path. Analogous to (1.6), the defining relation for the one-dimensional probe data is

$$\langle X^2 \rangle = 2 \int_0^\infty \Phi(K) \frac{dK}{2\pi}, \quad (1.7)$$

where the angle brackets denote an ensemble average. That is, a realization of the process based on estimates of its underlying spectral characteristics should preserve the relation between the second

moment and the integrated spectral intensity. For uniform spatial-frequency sampling, the proper scaling is  $2\pi PSD_n/\Delta K$ . In Part 1 of PL-TR-96-1084, Equation (6-11) defines (after an erroneous square root has been removed) the one-sided temporal-frequency PSD

$$\mathcal{G} = \frac{8}{3} \frac{2|dZ(f)|^2}{\Delta f}, \quad (1.8)$$

where  $\Delta f = 1/(N\Delta t)$  and the factor  $8/3$  provides the renormalization that preserves (1.6) for the Hanning window. In our notation,  $|dZ(f_n)|^2 \sim PSD_n$ . The frequency-interval scaling defines the units; however, there is no convention for indicating radian units for spatial frequencies. Radians per meter will be used throughout this report.

### 1.2.3 Scale spectra versus conventional spectra

There is considerable interest in wavelet scale spectra as an alternative to the DFT-based estimation just described. The data-probing power of wavelet-based analysis is discussed in Part 2. Here, we concentrate on the relation between the scale spectrum derived by averaging the wavelet detail coefficients over the delay variable and the periodogram estimate. This type of analysis is usually developed by using the scaled “mother” wavelet. Here we present a complementary analysis based on the discrete wavelet transform as derived from the low-pass and high-pass filter coefficients that generate, respectively, the wavelet scale function and the wavelet function itself.

To set up the problem, let  $x_k$  represent a sequence of discrete random variables. From Section 1.2.2, the raw periodogram estimate of the PSD is

$$P_n = \frac{1}{N^2} |\hat{x}(n)|^2, \quad (1.9)$$

where

$$\hat{x}(n) = \sum_{k=0}^{N-1} x_k \exp\{-2\pi i n k/N\} \quad (1.10)$$

is the DFT of  $x_k$ . For a homogeneous process,  $x_k$  admits the spectral representation

$$x_k = \int_{-K_N}^{K_N} \exp\{iKk\Delta x\} dZ(K), \quad (1.11)$$

where  $dZ(K)$  has the formal orthogonal-increments property

$$\langle dZ(K)dZ^*(K') \rangle = \delta(K - K') \Phi(K)/(2\pi). \quad (1.12)$$

Without loss of generality, we can assume either that the spectrum has no content beyond  $K_N = \pi/\Delta x$ , or that any content beyond the Nyquist range has been “aliased” into the Nyquist range. Using the orthogonal-increments property followed by some straightforward manipulations, it can be shown that

$$\langle P_n \rangle = \int_{-\infty}^{\infty} \frac{\sin^2 \left[ \frac{N}{2}(K - n\Delta K)\Delta x \right]}{N^2 \sin^2 \left[ \frac{1}{2}(K - n\Delta K)\Delta x \right]} \Phi(K) \frac{dK}{2\pi} \approx \Phi(n\Delta K), \quad (1.13)$$

where  $\Delta K\Delta x = 2\pi/N$ . The approximation holds with increasing  $N$  for  $n$  fixed at any value within its range. If a properly normalized weighting function had been used, a similar relation involving a more complicated spectral smoothing operation would result. Either way, for the purposes of

calculating averages of quantities involving periodogram estimates, the DFT coefficients admit the following approximate orthogonal-increments property:

$$\langle \hat{x}(n) \hat{x}^*(n') \rangle \approx N \langle P_n \rangle \delta_{n-n'}, \quad (1.14)$$

Effectively, we are assuming that any bias introduced by the weighting function is negligible for the class of power-law spectra that are being investigated.

We now consider the multi-scale-filtering representation of the discrete wavelet decomposition. If  $s_l$  and  $h_l$  represent, respectively, the average and detail filter coefficients associated with a wavelet scale function, the following recursion defines  $a_k$  and  $d_k^j$ . The latter is the discrete wavelet decomposition at scale  $j$ :

$$a_k^0 = x_k \text{ for } k = 0, \dots, N-1 \text{ where } N = 2^M.$$

For  $j = 1, \dots, M$  with  $k = 0, \dots, 2^{M-j} - L + 1$

$$a_k^j = \sum_{l=0}^{L-1} s_l a_{2k+L-1-l}^{j-1} \quad (1.15)$$

$$d_k^j = \sum_{l=0}^{L-1} h_l a_{2k+L-1-l}^{j-1} \quad (1.16)$$

From the inverse of (1.10), it follows that

$$a_k^0 = \frac{1}{N} \sum_{n=0}^{N-1} \hat{x}(n) \exp\{2\pi i n k / N\}. \quad (1.17)$$

Substituting (1.17) into (1.15) and (1.16) for  $j = 1$  yields

$$\begin{Bmatrix} a_k^1 \\ d_k^1 \end{Bmatrix} = \frac{1}{N} \sum_{n=0}^{N-1} \begin{Bmatrix} \hat{s}(n) \\ \hat{d}(n) \end{Bmatrix} \hat{x}(n) \exp\{2\pi i n k / (N/2)\}, \quad (1.18)$$

where

$$\begin{Bmatrix} \hat{s}(n) \\ \hat{d}(n) \end{Bmatrix} = \sum_{l=0}^{L-1} \begin{Bmatrix} s_l \\ h_l \end{Bmatrix} \exp\{-2\pi i n l / N\} \exp\{2\pi i n (L-1) / N\}. \quad (1.19)$$

To obtain a relation that contains only discrete spectral domain quantities, we substitute (1.18) into (1.15) and (1.16). For  $j = 2$ , the “new” spectral representation of the weighting coefficients effectively involves an  $N/2$  point DFT extended to  $N$  by periodic repetition. Thus, by induction, for  $j = 2, \dots, M$  with  $k = 0, \dots, 2^{M-j} - (L-1) + (L-2)/2^j$ ,

$$d_k^j = \frac{1}{N} \sum_{n=0}^{N-1} \hat{S}(n; j) \hat{x}(n) \exp\{2\pi i n k / 2^{M-j}\}, \quad (1.20)$$

where

$$\hat{S}(n; j) = \hat{d}(n/2^{j-1}) \prod_{l=0}^{j-2} \hat{s}(n/2^l). \quad (1.21)$$

Equation (1.20) describes the recursion leading to the detail coefficients as a scale-dependent filtering operation. In (1.21), the product term represents the successive low-pass-filtering and down-sampling followed by repetition of the surviving coefficients to maintain  $N$  terms.

The wavelet scale spectra are obtained by forming the sample average

$$S_j = \frac{1}{N_j} \sum_{k=1}^{N_j} (d_k^j)^2$$

where  $N_j$  represents the number of detail coefficients available at scale  $j$ . The result is independent of  $k$ , but difficult to interpret. To the extent that (1.14) is valid, however, it follows that

$$\langle (d_k^j)^2 \rangle = \frac{1}{N} \sum_{n=0}^{N-1} |\hat{S}(n; j)|^2 \langle P_n \rangle.$$

In the same way that the standard spectral weighting is used to extract an estimate of the PSD, if  $|\hat{S}(n; j)|^2$  is concentrated around  $2^{-j+1}\Delta K$ , the scale spectrum should be proportional to the power spectral density evaluated at  $2^{-j+1}\Delta K$ . Figure 1.1 shows the filter functions through scale 7 for the Haar wavelet. The first four scales are superimposed and plotted against a uniform frequency scale. The remaining wavelets are plotted individually against a logarithmic frequency scale to show the low-frequency behavior more clearly. Each filter has its peak at  $K_N/2^{j-1}$ , although the  $j = 1$  filter is half-band in its frequency response. For comparison, Figure 1.2 shows the corresponding filters for the db5 wavelet.

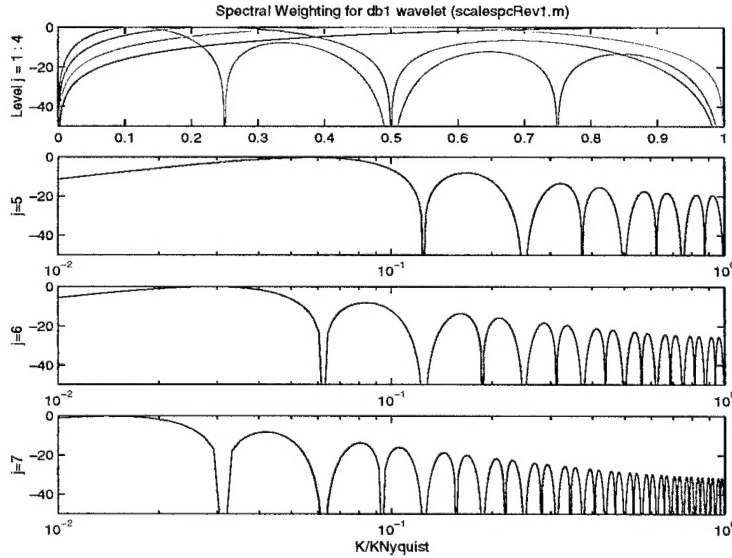


Figure 1.1: Spectral filter functions for Haar wavelet with 1024 points. Only the positive frequencies are shown, and each filter is normalized to unity at its peak value.

Because of the complexity of the scale filters, it is difficult to make a general statement about the precise relation between the expectation of the scale spectrum and the expectation of the periodogram. To investigate this relation, we have made comparisons between PSD and wavelet-scale spectra applied to simulated data. We have also evaluated the wavelet spectral filter functions for the theoretical form of the spectral-density function used to generate the simulated data to which the wavelet and PSD analyses were performed. Figures 1.3 and 1.4 show wavelet scale spectra results for the db1 (Haar) and db5 wavelets. With Haar, the measured wavelet, the theoretical average

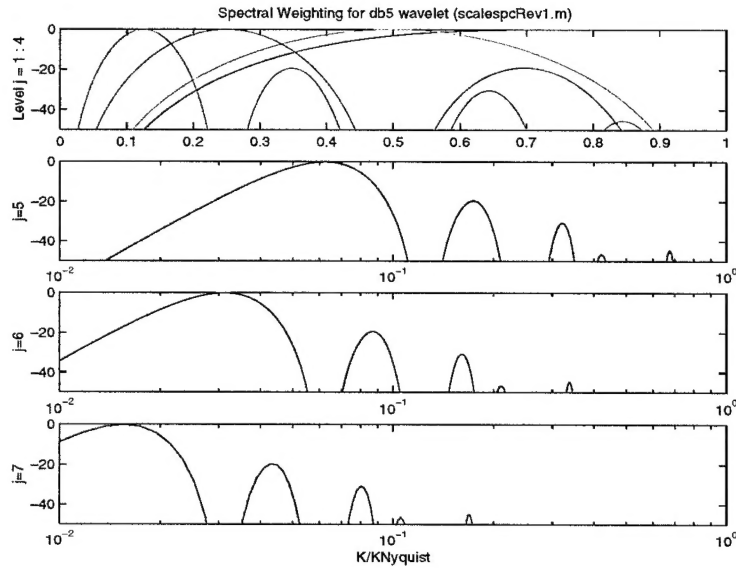


Figure 1.2: Spectral filter functions for db5 wavelet for comparison to Haar wavelet shown in Figure 1.1.

scale spectra estimate, and the theoretical spectra agree quite well. For the db5 wavelet there is a scale-dependent bias between the theoretical and measured scale spectra that is not reproduced by the theoretical computations. If the theoretical computation of the filter coefficients is in error, it is possibly due to an inadequate representation of the filter functions at the logarithmic sample intervals. The filter functions for the wavelet at scale nine is superimposed on each plot. We see that the sidelobes are not critically sampled.

To complete our evaluation of the parameter estimation procedures, we compare the parameter estimates as extracted from log-linear-least-squares fits applied to standard PSD estimates and to Haar wavelet scale spectra. In all cases, the biases in the slopes were found to be quite small. The strength parameter, however, is more complicated. The PSD estimates exhibit a bias that varies systematically with the number of blocks averaged prior to applying the parameter extraction. The overall bias also depends on the weighting function. This characteristic is evidently known, and it is clear that it is caused by the complicated statistical fluctuations introduced by the nonlinear logarithmic operation applied to the spectral estimates prior to the linear least-squares curve fitting. Figure 1.5 summarizes the results for both the PSD-based and Haar wavelet scale spectra results. The Haar wavelet scale analysis produced a small (less than 0.2 dB) fairly uniform bias up to eight-block averages. Beyond that the available range of unambiguously sampled wavelengths evidently begins to affect both the standard and the wavelet scale spectra. Because of the desire to maintain high resolution with as little bias as possible, the Haar wavelet scale spectra were used for the analysis of the parameter fluctuation process as presented in Part 2.

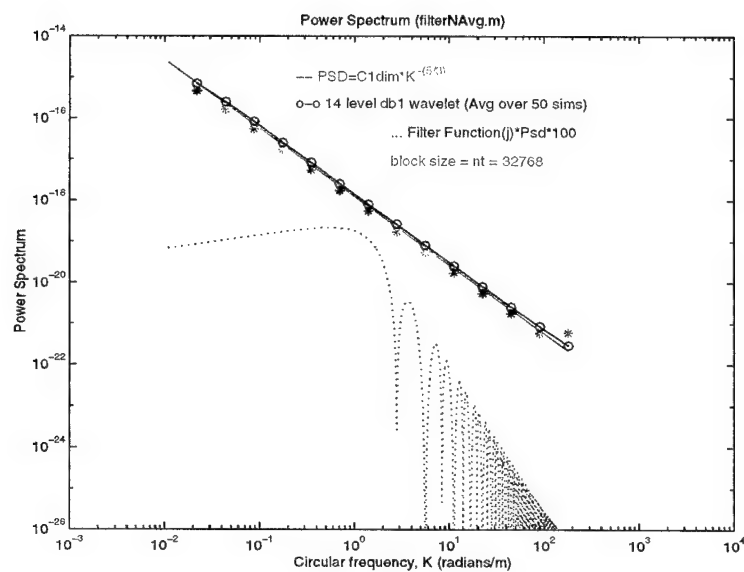


Figure 1.3: Comparison of periodogram and scale-spectrum PSD estimates for db1 wavelet.

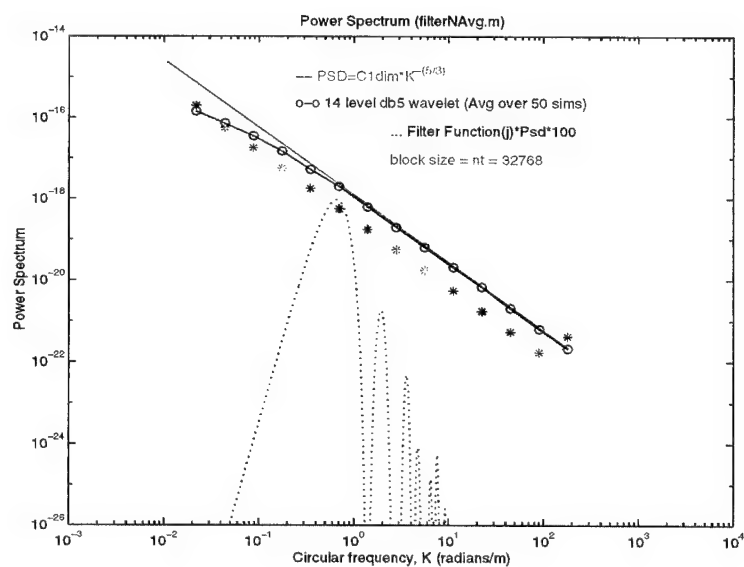


Figure 1.4: Comparison of periodogram and scale-spectrum PSD estimates for db5 wavelet.

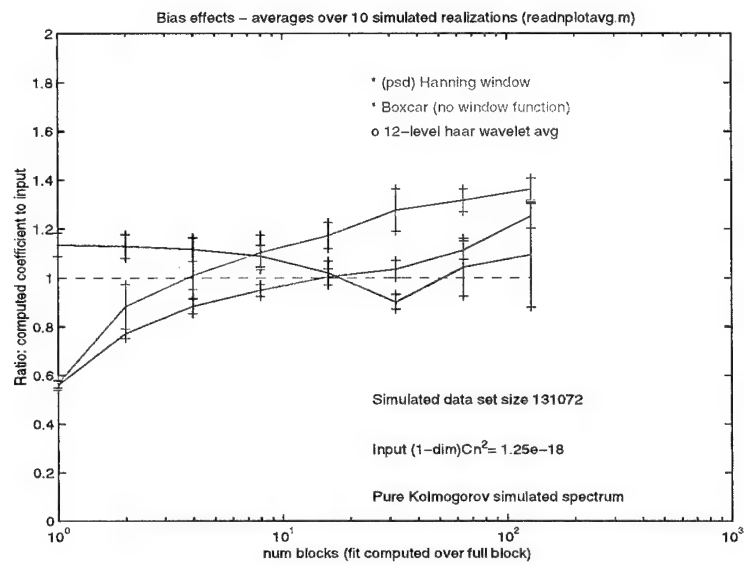


Figure 1.5: Comparisons of strength parameter estimates from standard spectral estimators and wavelet scale spectra.



### 1.3 Analysis of file 95135-04 data

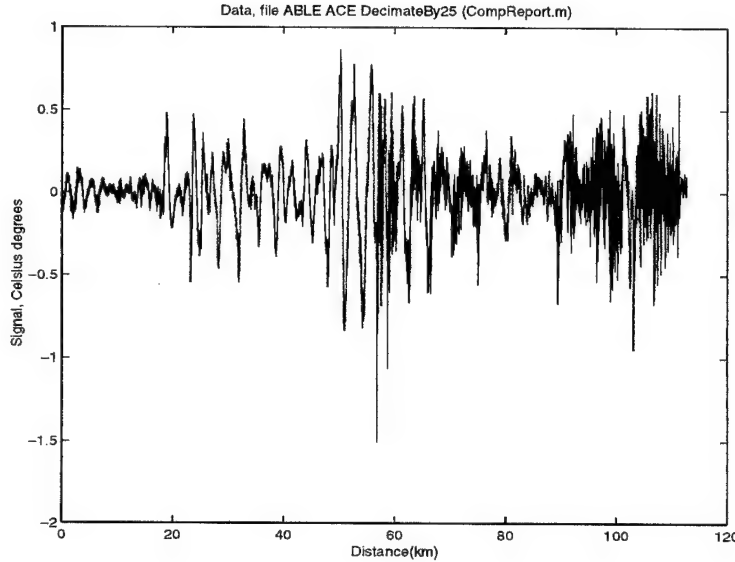


Figure 1.6: Overview of temperature fluctuation data from file 95135-04.

The data from file 95135-04 have been targeted for in-depth analyses by different research groups. Figure 1.6 shows the data set in its entirety but decimated by 25 samples for more efficient display. The data show structure on varying scales up to the 4-km large-scale (low-frequency) cutoff of the temperature-probe filter. Irrespective of any other consideration, we observe the abrupt increase in the intensity of the small-scale structure at distances beyond 60 km. To capture the transition, a segmentation length of one kilometer is needed. To probe the structure at low spatial frequencies, Figure 1.7 shows a PSD obtained from the entire decimated data set shown in Figure 1.6. A prominent feature is the low-frequency enhancement beginning near the low-frequency filter cutoff. The enhancement extends downward to spatial frequencies approaching  $2\pi$  radians/km. The wavelet analysis presented in Part 2 isolates this structure, which we believe to be spurious, but for our purposes here we simply note that the spectral components approaching  $2\pi \times 10^{-3}$  radians/meter are suspect and should be avoided for parameter estimation.

We also note the narrow spectral line at the spatial frequency corresponding to 1.2 m. This feature is also suspect, but we shall see that it is well outside the range where extraction of turbulence-related parameters is meaningful.

#### 1.3.1 Analysis by data sub-segment

Based on the preliminary survey of the data, PSD estimates were performed with block sizes of  $2^{13} = (163.8 \text{ m})$ ,  $2^{14} (327.6 \text{ m})$ ,  $2^{15} (655.36 \text{ m})$  and  $2^{16} (1.31 \text{ km})$ . Figure 1.8 shows the sliding least-squares estimates of the power-law index and structure-constant parameters obtained from the first 50 km of one 10-km segment within the data set. Each data point corresponds to the one-decade estimate centered on the spatial wave number at which it is plotted. The data fits are obtained from averages of the sub-segment PSD estimates. The longer block lengths provide more low-frequency information but poorer stability, since fewer blocks are available for averaging. The horizontal dashed line in the upper frame corresponds to the Kolmogorov value. In the lower

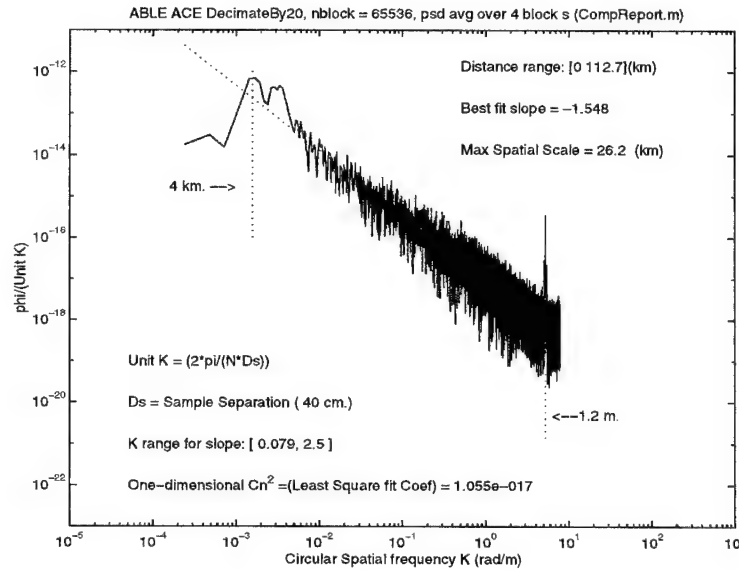


Figure 1.7: PSD estimate derived from 20:1 decimation of file 95135-04 data after conversion to refractive index fluctuation units.

frame, the dashed line indicates the “clear” level at which significant system effects can occur. The spectra all show shallowing (less negative index parameters) at  $K = 2$  rad/m followed by a steepening at higher spatial wave numbers. The dependence of the results on segmentation shows that the power-law characteristics in the low-frequency range are not well defined.

The results of applying the same parameter extraction procedure to the second 50-km segment are shown in Figure 1.9. The strength of turbulence has increased by more than an order of magnitude, which exposes a consistent power-law regime between  $K=1$  and 5 rad/m. Figures 1.10 and 1.11 show the least-squares fits from sliding two-decade ranges as obtained from the  $2^{15}$  blocks. The same general characteristics are observed, although the slope estimates derived from the first data segment are more erratic when measured over the two-decade range.

In a power-law environment it is desirable to isolate a spatial-frequency range within a uniform portion of the power-law region for parametric study. This procedure is compromised by the lack of clean power-law definition in the initial 50 km of the data set. Thus, in Figure 1.12 the same block was analyzed with the two-decade window split into upper (red) and lower (blue) one-decade segments. The selected range for power-law extraction is  $K=0.5$  to 5 rad/m. The two-decade fit (green) is replotted for reference. From a physics viewpoint, one might expect a smooth low-frequency reservoir to feed the developing turbulence. The average spectral characteristics shown in Figure 1.13 suggest this behavior. Thus, the upper curve captures some of the steepening while the lower curve and the overall average capture the shallower central segment of the spectrum. The objective of obtaining a single power-law fit is best met by the shallower power law.

For completeness, Figure 1.14 shows the average PSD for one segment within the second 50-km portion of the data. Here the power-law parameters are consistent and the index is near the Kolmogorov value. We note, however, that the lowest frequencies depart from the Kolmogorov limit by first developing a shallow ledge and then steepening. The contamination of the data at low spatial wave numbers compromises any phenomenological interpretation of this result.

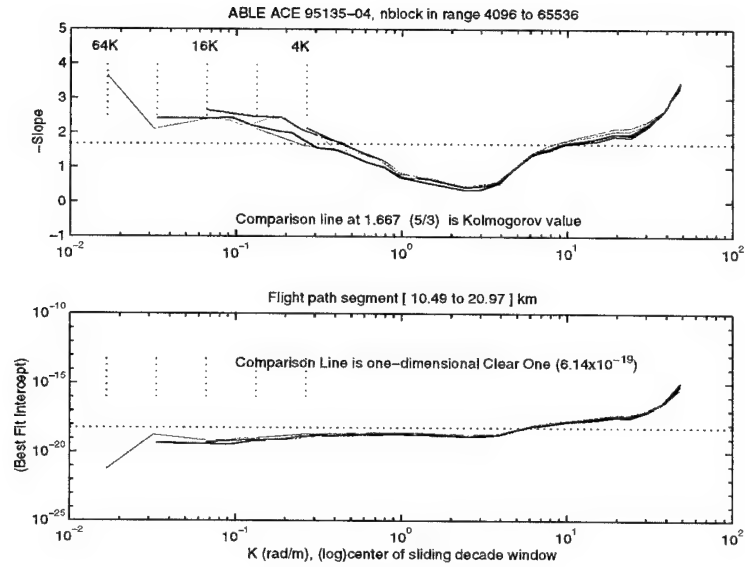


Figure 1.8: Power-law fit parameters (top slope/bottom intercept) derived from one-decade sliding window using average spectra with different block sizes applied to first 50-km segment.

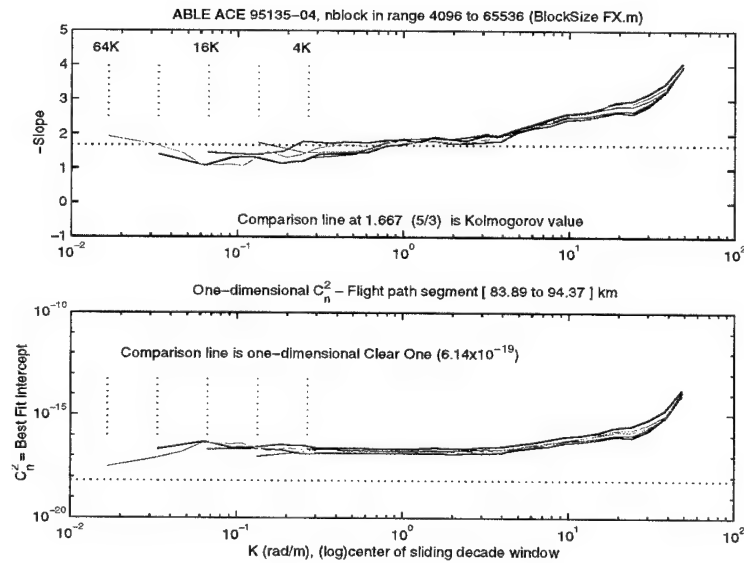


Figure 1.9: Power-law fit parameters derived from one-decade sliding window using average spectra with different block sizes applied to second 50-km segment.

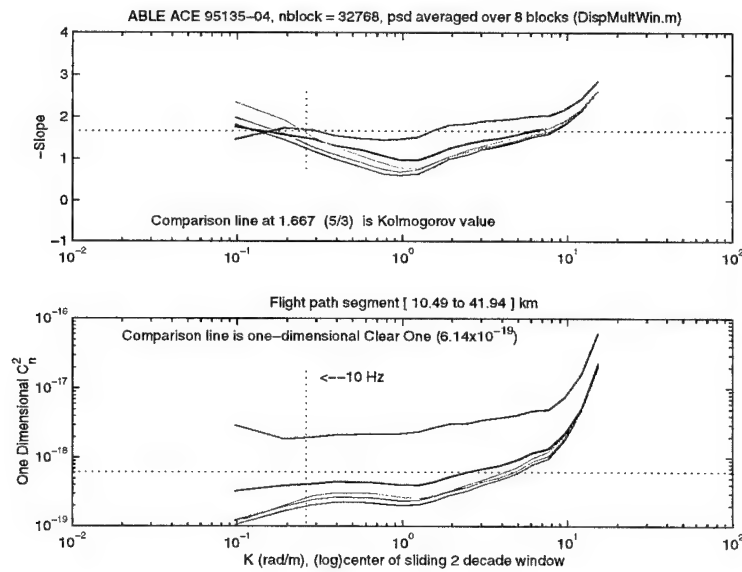


Figure 1.10: Power-law fit parameters derived from two-decade sliding window using spectra from eight  $2^{15}$  sample blocks within the first 50-km segment.

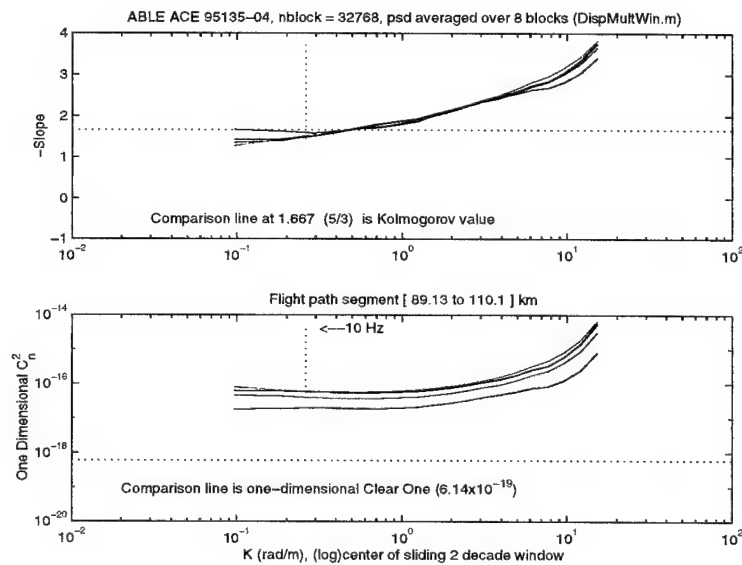


Figure 1.11: Power-law fit parameters derived from two-decade sliding window using spectra from eight  $2^{15}$  sample blocks within the second 50-km segment.

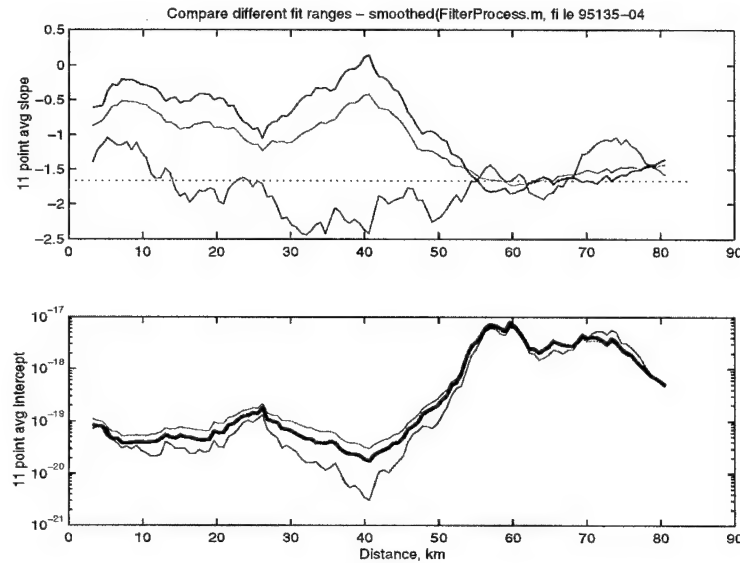


Figure 1.12: Power-law fit parameters derived from different spectral windows using spectra from individual  $2^{15}$  blocks over the entire data set.

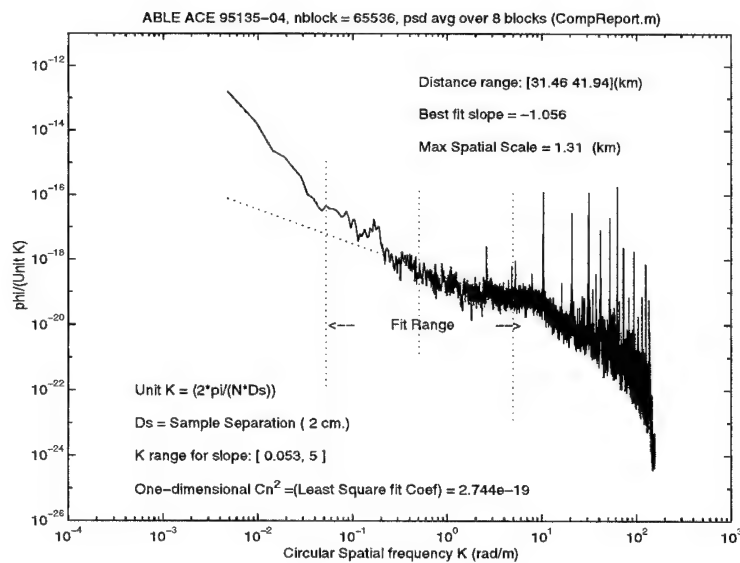


Figure 1.13: PSD estimate from the first 50-km segment derived by averaging a typical set of eight PSD estimates from  $2^{16}$  blocks.

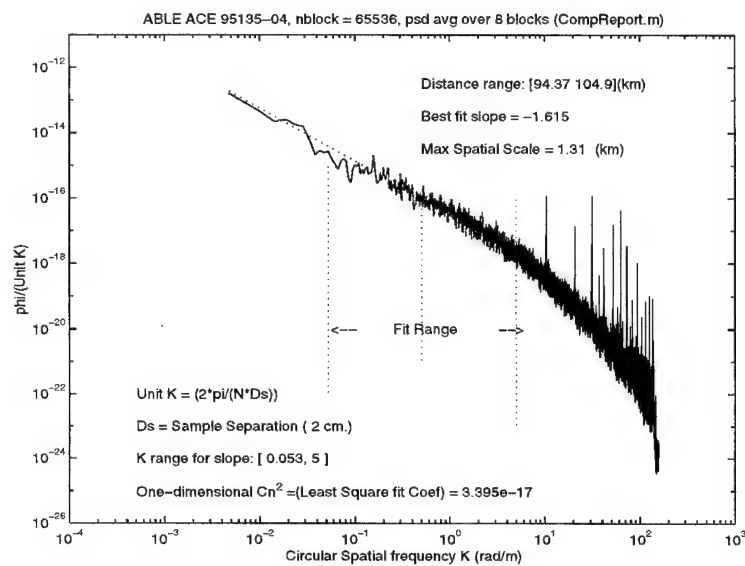


Figure 1.14: PSD estimate from the second 50-km segment derived by averaging a typical set of eight PSD estimates from  $2^{16}$  blocks.

### 1.3.2 Variability of power-law parameters from fixed wave number ranges

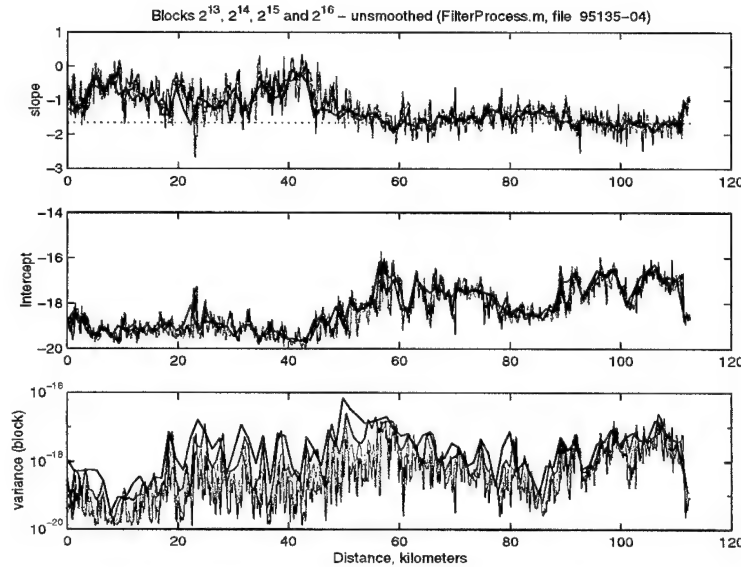


Figure 1.15: Power-law fit and variance parameters derived from fixed two-decade window applied to contiguous blocks over the entire data set.

Figure 1.15 shows single-block power-law fit parameters derived from contiguous segments over the whole data set. The superimposed curves are for different block sizes and thereby show increasing levels of detail in the parameter estimates. The average spectral characteristics derived from a fixed spatial frequency range are not affected by block size because the largest scale used for parameter extraction is captured by the smallest block. The lower frame shows the second moment of the fluctuations, which is equal to the integral of the PSD. The second-moment data show an increase with block size and a higher overall variability because of the mix of structure involved.

As noted in Section 1.2.3, the Haar wavelet provides an intrinsically smoothed version of the PSD estimator that faithfully follows the PSD estimate for a uniform power-law segment. Figures 1.16 and 1.17 show a comparison of the standard and wavelet-scale estimators at two segment lengths. In general, the wavelet-scale-spectrum-based parameters are smoothed versions of the periodogram-spectrum-based estimators; however, in the weak turbulence regime there is a small disparity in the structure constant estimate. This may be due to logarithmic sampling effects as discussed in Section 1.2.3. For the db5 wavelet as shown in Figure 1.18, however, there is a systematic bias consistent with our observations of simulated data.

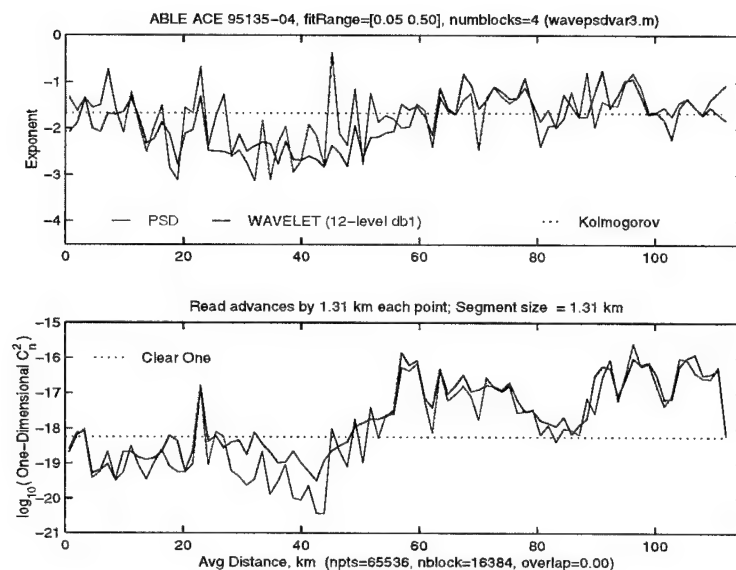


Figure 1.16: Comparison of wavelet-scale-spectrum-based estimator to the periodogram-based estimator for Haar wavelet at 1.1-km resolution.

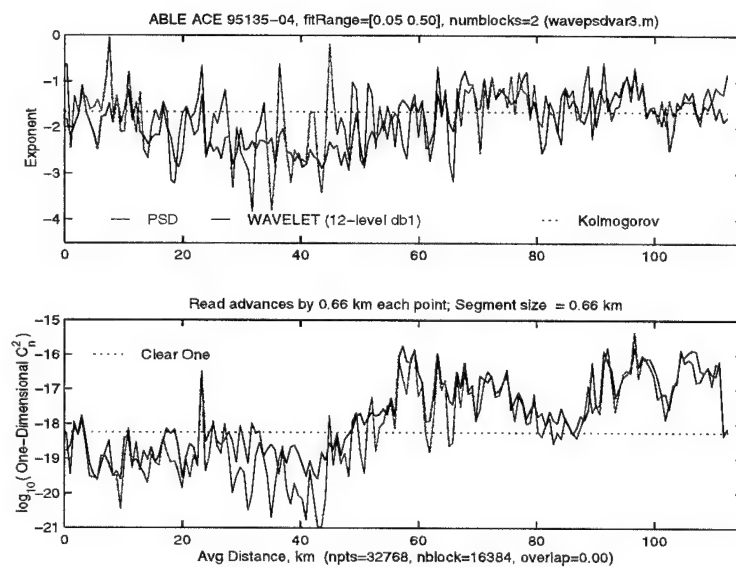


Figure 1.17: Comparison of wavelet-scale-spectrum-based estimator to the periodogram-based estimator for Haar wavelet at 0.6-km resolution.



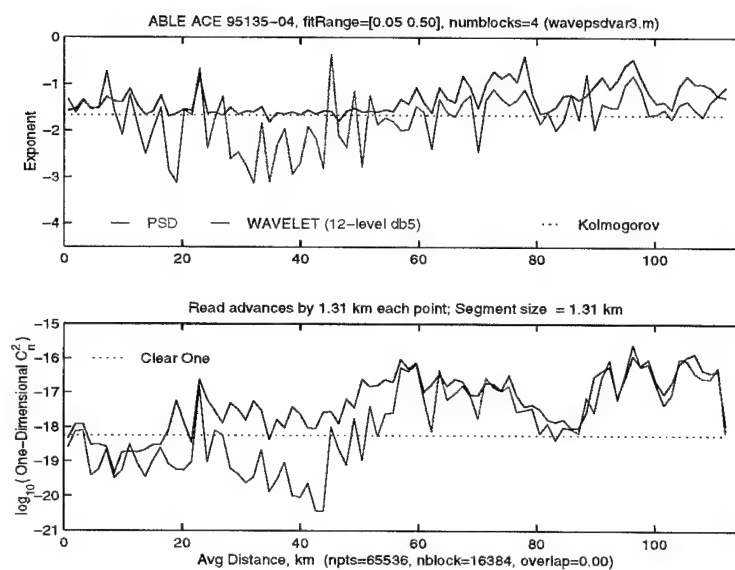


Figure 1.18: Comparison of wavelet-scale-spectrum-based estimator using db5 wavelet to the periodogram-based estimator from Figure 1.16.

## 1.4 Analysis of Bahrain Data

To demonstrate the robustness of our analysis procedure, we have applied it to two additional data sets that have been analyzed in detail by Phillips Laboratory. A full-resolution PSD from the first data set is shown in Figure 1.19. In this data set there is a high spatial wave number feature that we believe to be spurious. Thus, the spectral analysis window was set up over a narrower window, as indicated in Figure 1.19. Following the same procedure that was used for the 95135-04 data, the power-law index and strength of turbulence parameters were estimated using both PSD and Haar-wavelet scale spectra. The results for 1.2-km and 0.6-km segments are shown in Figures 1.20 and 1.21, respectively. There are differences in detail between these summary data and the corresponding summary analysis performed by Phillips Laboratory. We attribute these differences to the fact that overlapping data segments were used by Phillips Laboratory. Also, Phillips Laboratory used 16 block averages with linear trend removal. As already noted, to properly interpret the parameter fluctuations, we have avoided operations that remove any structure. Part 2 discusses our procedures for characterizing the noise structure.

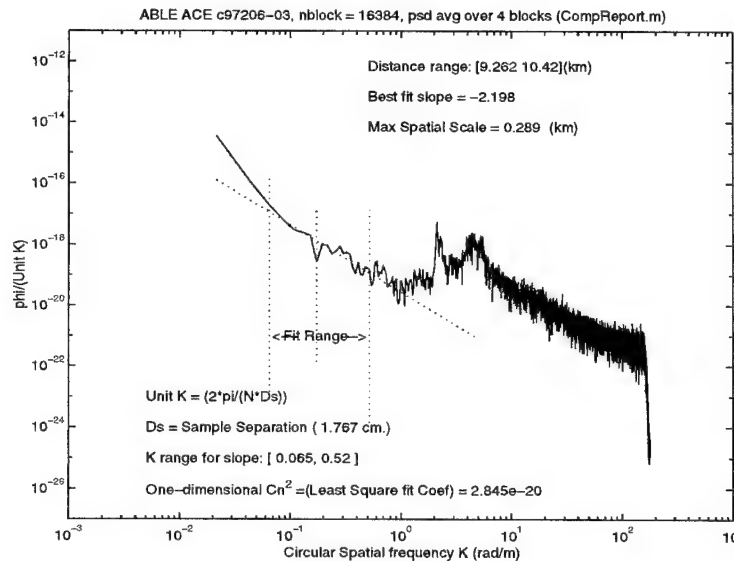


Figure 1.19: High-resolution PSD from Bahrain data set 97206-3.

Figures 1.22, 1.23, and 1.24 show a representative PSD and the parameters that result from applying the parameter estimation procedure to data set 97206-15. Here the turbulence is somewhat weaker and the limitations of the restricted spectral window that was available are influencing the parameter estimation. There are significant differences between the PSD and Haar-wavelet-scale-spectra estimates. The logarithmic sampling associated with the wavelet scale spectrum produces a sparse sampling of the available spectral window; moreover, there are significant departures from power-law behavior. This is a topic for further investigation, but for now we accept the biased wavelet estimate as the reference for analysis in Part 2.

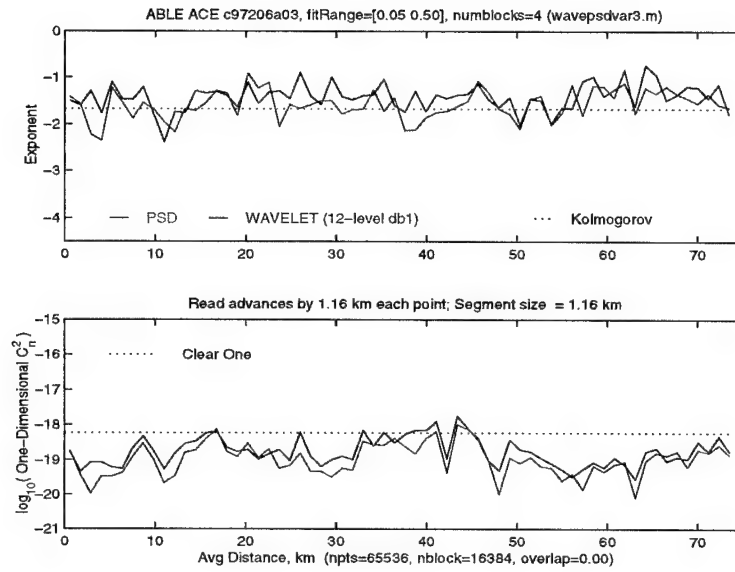


Figure 1.20: PSD and wavelet-scale parameter estimates from 97206-3 data set at 1.2-km segmentation length.

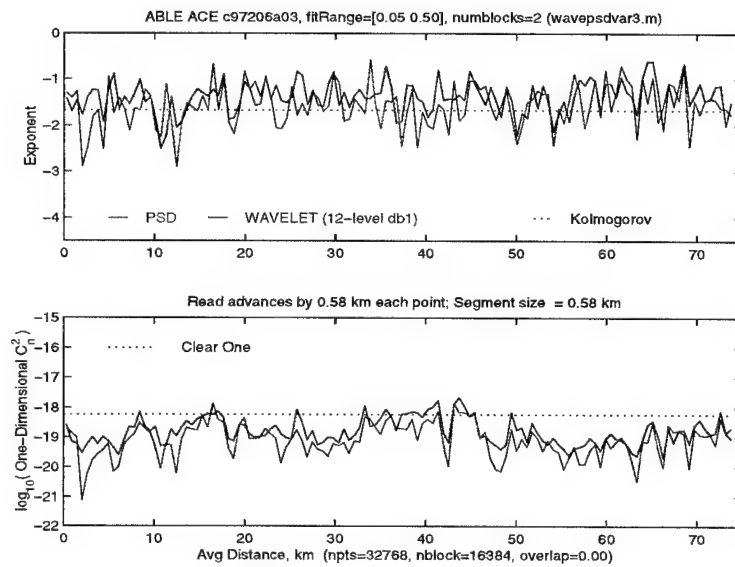


Figure 1.21: PSD and wavelet-scale parameter estimates from 97206-3 data set at 0.6-km segmentation length.

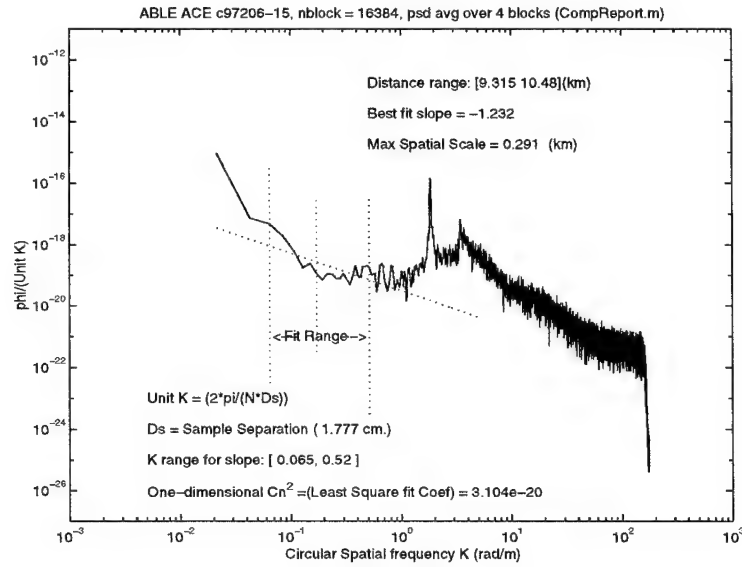


Figure 1.22: High resolution PSD from Bahrain data set 97206-15.

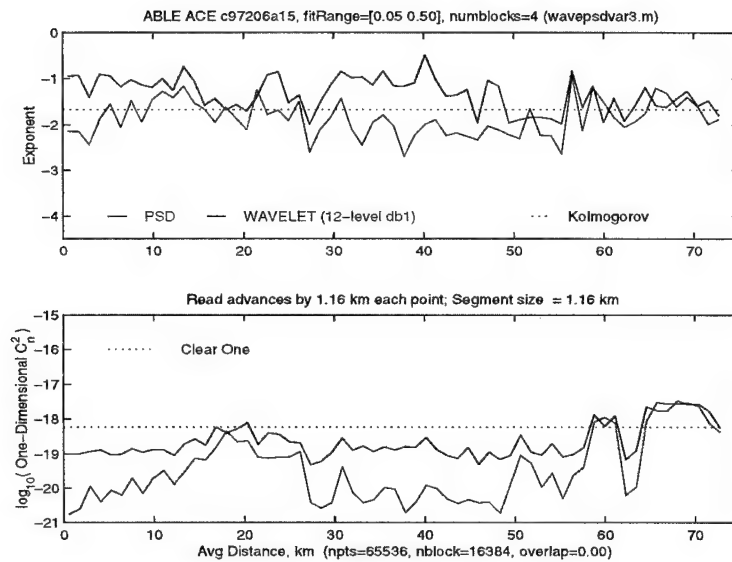


Figure 1.23: PSD and wavelet-scale parameter estimates from 97206-15 data set at 1.2-km segmentation length.

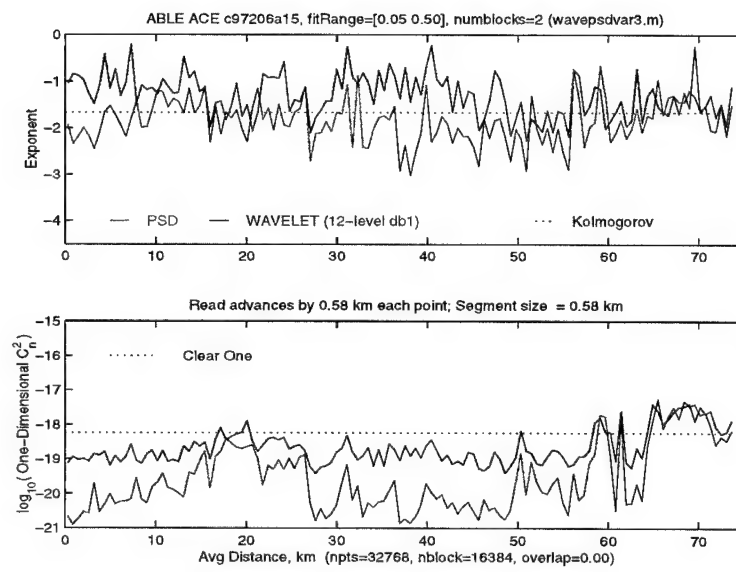


Figure 1.24: PSD and wavelet-scale parameter estimates from 97206-15 data set at 0.6-km segmentation length.

## 1.5 Summary

To summarize the results of the preliminary data analysis and parameter estimation, the parameter estimates from each file at the highest resolution of approximately 0.6 m are presented in histogram form. Figure 1.25 corresponds to the data presented in graphical form in Figure 1.17. Several features should be noted. First, the wavelet-scale-spectra parameters show less fluctuation. Secondly, the strong and the weak turbulence produce somewhat distinct populations in the turbulent strength histograms—one peaking below -18 log units and the other peaking between -17 and -16 log units. By comparison, the wavelet slope distribution is more uniform. This is an encouraging result in that one expects the slope parameter to be intrinsic to the turbulence process. Departures from the Kolmogorov limit would occur only because the data window did not encompass measurable turbulence in its inertial regime. Strength, by comparison, should reflect how strongly the turbulence is being driven. These observations apply to the expectation values of the parameters. The fluctuation process will be investigated in Part 2.

Similarly, the data presented in Figures 1.26 and 1.27 correspond, respectively, to the graphical presentations in Figures 1.21 and 1.24. These results show the same smoothing effect of the wavelet-scale-spectrum estimator, but the distributions are more erratic, reflecting the limited spectral range discussed above and the generally weaker turbulence levels encountered.

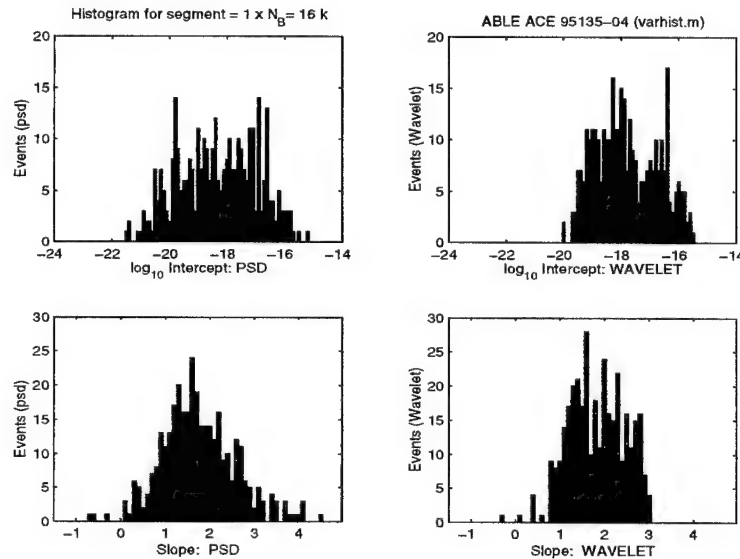


Figure 1.25: Histogram presentation of data from Figure 1.17.

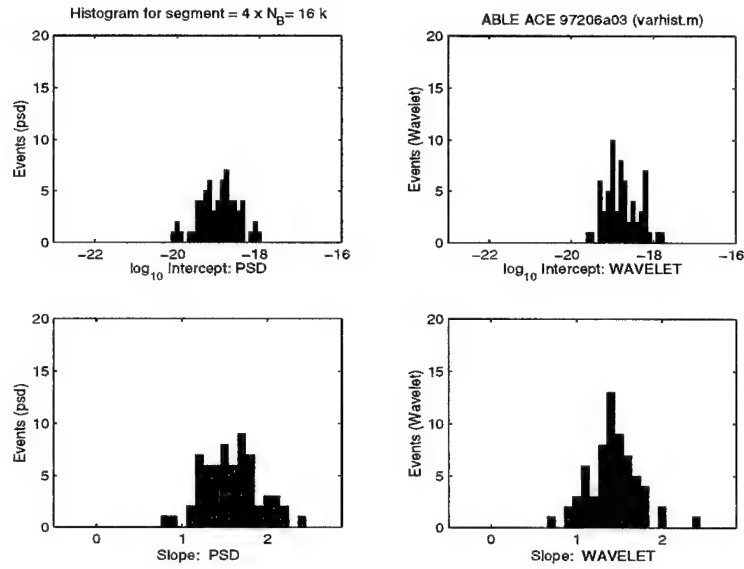


Figure 1.26: Histogram presentation of data from Figure 1.21.

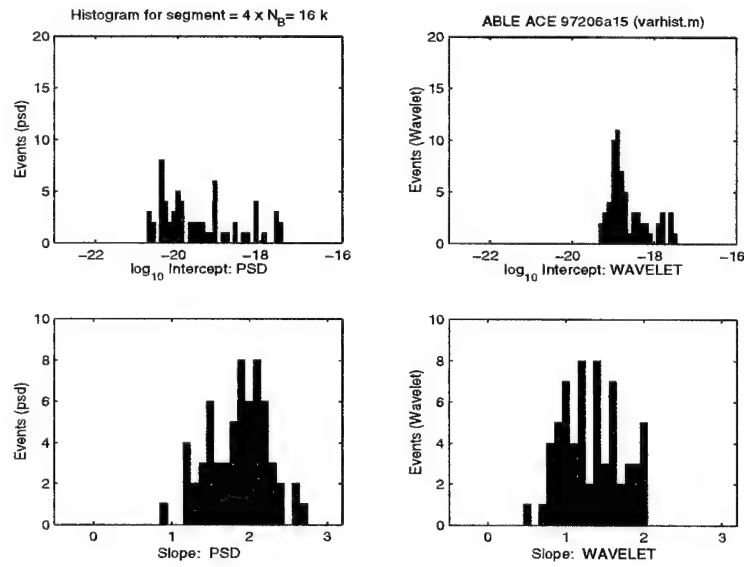


Figure 1.27: Histogram presentation of data from Figure 1.24.

## 2 Scale spectral analysis

The basic scaling theory of atmospheric turbulence tells us that, locally, the power spectral density of the temperature should have power law behavior over some range of scales. The aim of this study is to estimate this local power law behavior from the aerothermal data, allowing for variations over longer scales that are on the order of kilometers.

In Section 2.1 we introduce the data and note that they are corrupted by the measurement process. In Section 2.2 we introduce the scale spectral decomposition of the data, or of segments of it, and note qualitatively its power law form. We discuss different segmentations of the data and the way a power law is fitted to the scale spectra. In Section 2.3 we discuss how to assess and filter out the effects of segmentation and sampling variability in the scale spectra. We begin in Section 2.3.1 with a simulation of the temperature data as a Gaussian local power law process with the slope and log intercept obtained from the actual data and then smoothed (Figure 2.7). The estimation of the local power for the simulated data gives us a quantitative measure of fluctuations due to sampling and segmentation. In Section 2.3.2 we carry out a variogram analysis of the estimated slope and log intercept of the *actual* data. We assume that the variograms have a simple structure that depends on three parameters, and we estimate them. In Section 2.3.3 we use the estimated variogram model to filter out the sampling error in the slope and log intercept estimates. We find (Figures 2.14, 2.15 and 2.16) that this filtering process removes, to a large extent, segmentation effects over a large range of segmentation sizes. This filtering is a simple but important step in our analysis of the aerothermal data.

In Section 2.4 we show how to simulate faithfully the temperature data as a local power law process. In Section 2.4.1 we generate and analyze simulations which are locally Gaussian power-law processes over the full range of scales available in the actual data. The local power law that we use in the simulations is estimated one from the actual data, after filtering (as in Figure 2.14). In Section 2.4.2 we use replication to assess the standard deviation of the sampling error. In Section 2.4.3 we examine the effect on the estimation of the slope and log intercept of the range of scales of the spectrum that is used. This indicates that over a suitable range of scales a local power law model fits the data well. In Section 2.4.4 we simulate the temperature data with a Gaussian local power law process in which the slope and log intercept are themselves stochastic processes with statistical properties determined by the actual data, as in Section 2.3.2 and the smooth background of Figure 2.7. In Section 2.4.5 we use replication to estimate the standard deviation of the sampling error in the slope and log intercept process. We find that it is nearly twice as large as the corresponding one of Section 2.4.2 where the simulations use the actual estimates of the slope and log intercept.

In Section 2.5 we summarize our analysis and conclusions. Our main result is that the atmospheric temperature data that we studied can be modeled very well by a *local* power law process. The slope and log intercept of the local power law spectrum can be estimated accurately and are essentially independent of the segmentation used.

### 2.1 The data

In Figure 2.1 (top) we show the temperature data, which is composed of 5,636,096 data points and is plotted subsampled 1/50. In Figure 2.1 (bottom) we show the consecutive differences of the temperature, subsampled 1/50. It is clear from the difference figure that there is a very pronounced periodic component in the data, with period of about 4 km (20 sec). In Figure 2.2 we show two 2km segments of the data, one (top) beginning at the 2-km point and the other (bottom) beginning at the 108-km point. Figure 2.3 is the same as Figure 2.2 except that temperature differences are shown. Note the smaller-amplitude, regular periodic pattern with period of about 60 m and the



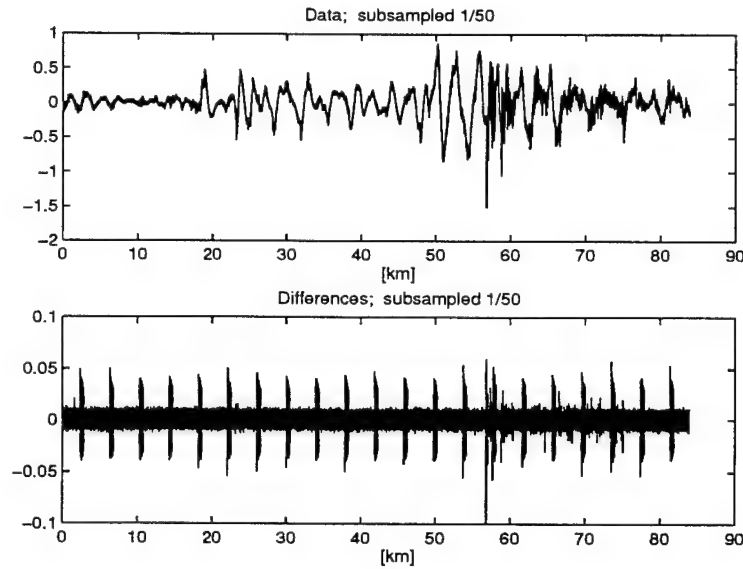


Figure 2.1: Top frame: the raw temperature data over the first 84 km out of a 112 km record, subsampled 1/50. The spatial resolution of the data is approximately 2 cm. Bottom frame: successive temperature differences for the same 84km data set, subsampled 1/50. Note the systematic burst in the temperature differences, with a period of about 4 km

larger-amplitude pattern of about 500 m, which is the blown-up view of the 4-km blip in Figure 2.1. This larger-amplitude pattern has an internal periodic structure of about 60 m.

It is clear from Figures 2.1, 2.2 and 2.3 that the temperature data are not a stationary time series and do not have stationary increments (differences). However, the increments have a more regular structure and the embedded periodic components are more visible in the difference plot. It is also clear that the visible periodic structures in the data cannot be attributed to turbulence, or larger coherent structures in the atmosphere, because of the precise periodicity over the full 112-km length of the data set. The estimation of the effects of atmospheric turbulence must seek to suppress these spurious features.

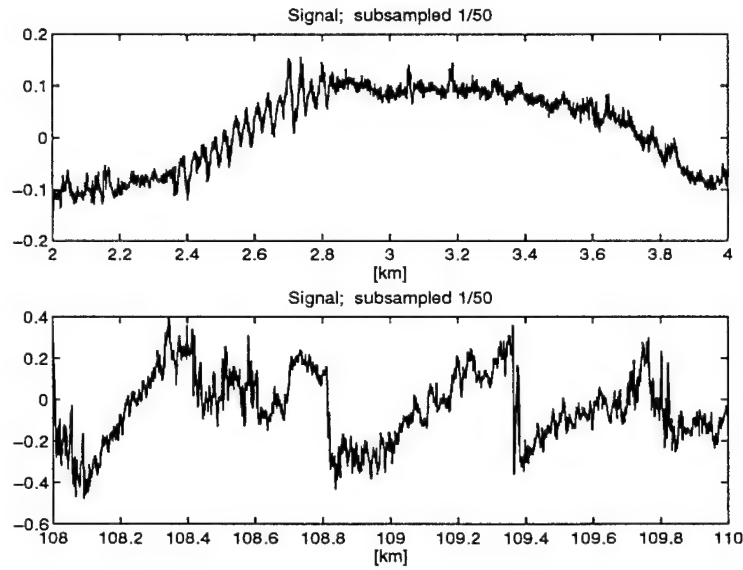


Figure 2.2: Top frame: the temperature data between 2 km and 4 km, subsampled 1/50. The segment between 2.4 km and 2.8 km corresponds to a burst. Bottom frame: the temperature data between 108km and 110km. There is a burst between 109 km and 109.4 km but it is not so visible in this plot.

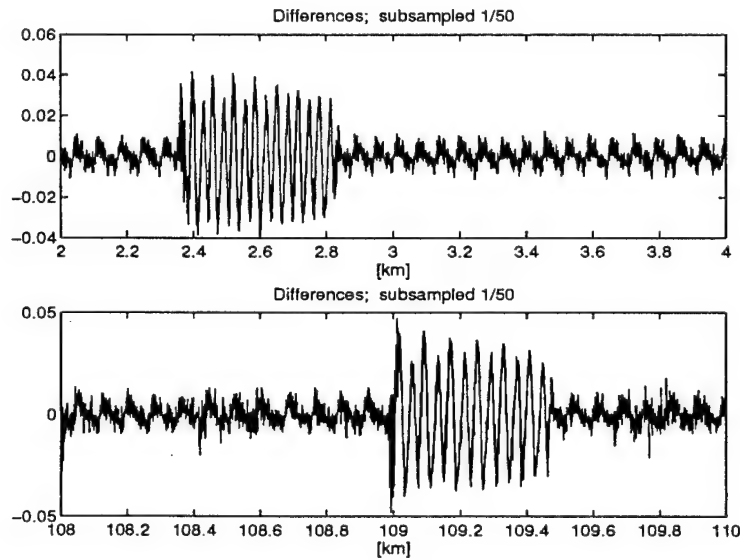


Figure 2.3: The top and bottom frames here are successive temperature differences for the two segments in Figure 2.2. Note that the internal structure of the burst has a repeating pattern with a 50- to 60-m period. There is, in addition, a lower amplitude, 50- to 60-m periodic pattern in the rest of the data.

## 2.2 The wavelet analysis

Let  $X = (a_0(1), a_0(2), \dots, a_0(2^M))$  denote the temperature data. It is convenient to work with data vectors whose length is a power of two because computations are faster for them. In our case  $M$  is between 22 and 23 and we shall work typically with vectors of length  $2^{22} = 4194304$ , corresponding to the first 84-km section of the 112-km data set. We want to carry out a spectral analysis of  $X$  and to fit the estimated power spectral density to a power law. For this purpose *scale* spectra, rather than Fourier spectra, are a more flexible tool and we will use them here [1].

From the signal, we construct successively its wavelet coefficients with respect to the Haar basis as follows. Let

$$a_1(n) = \frac{1}{\sqrt{2}}(a_0(2n) + a_0(2n-1)) \quad (2.1)$$

$$d_1(n) = \frac{1}{\sqrt{2}}(a_0(2n) - a_0(2n-1)) , \text{ for } n = 1, 2, \dots, 2^{M-1} \quad (2.2)$$

be the smoothed signal and its fluctuation, or detail, at the finest scale. Note that the detail vector  $d_1$  contains every other successive difference of the data. This process of averaging and differencing can be continued by defining

$$a_2(n) = \frac{1}{\sqrt{2}}(a_1(2n) + a_1(2n-1)) \quad (2.3)$$

$$d_2(n) = \frac{1}{\sqrt{2}}(a_1(2n) - a_1(2n-1)) , \text{ for } n = 1, 2, \dots, 2^{M-2} \quad (2.4)$$

and in general

$$a_k(n) = \frac{1}{\sqrt{2}}(a_{k-1}(2n) + a_{k-1}(2n-1)) \quad (2.5)$$

$$d_k(n) = \frac{1}{\sqrt{2}}(a_{k-1}(2n) - a_{k-1}(2n-1)) , \text{ for } n = 1, 2, \dots, 2^{M-k} \quad (2.6)$$

for  $k = 1, \dots, M$ . The data vector  $X$  can then be reconstructed from  $a_M, d_M, d_{M-1}, \dots, d_1$  since from (2.1) we have

$$a_0(2n) = \frac{1}{\sqrt{2}}(a_1(n) + d_1(n)) \quad (2.7)$$

$$a_0(2n-1) = \frac{1}{\sqrt{2}}(a_1(n) - d_1(n)) , \text{ for } n = 1, 2, \dots, 2^{M-1} \quad (2.8)$$

and now  $a_1$  can be replaced by sums and differences of  $a_2$  and  $d_2$ , etc.

In Figure 2.4 we show the first 21 km of the temperature data ( $M = 20$ ) along with  $d_1, d_3, d_5, d_7, d_9, d_{11}, a_{12}$ . Note the similarity between  $d_1$ , and to some extent  $d_2$ , and the successive differences in Figure 2.1, bottom. The detail coefficients  $d_k$  carry information about the data on longer scales, as  $k$  increases. For example,  $d_7$  shows successive differences of the temperature over a distance of 2.56 m, after averaging over successive segments of length 1.28 m.

The scale spectrum of  $X$ , relative to the Haar wavelet basis, is the sequence  $S_j$  defined by

$$S_j = \frac{1}{2^{M-j}} \sum_{n=1}^{2^{M-j}} (d_j(n))^2 , \quad j = 1, 2, \dots, M \quad (2.9)$$

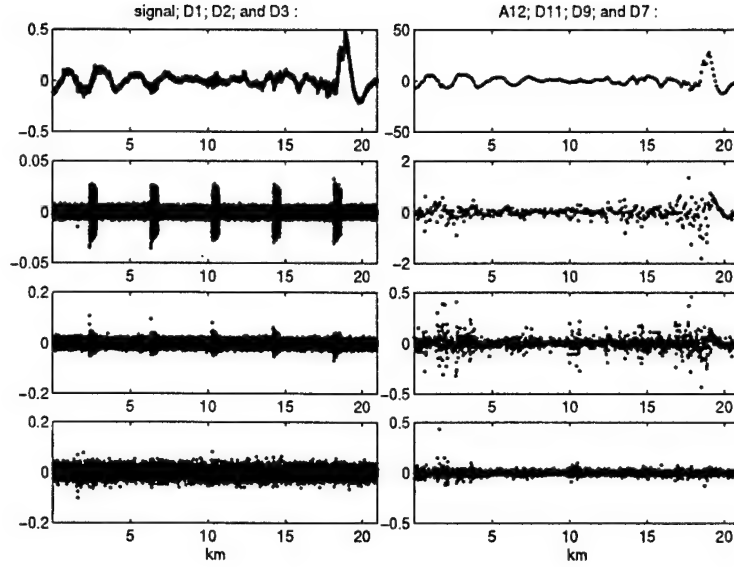


Figure 2.4: Haar wavelet coefficients for the first 21 km of the data. The top left frame is the temperature data. The one below it is the  $d_1$  detail coefficients (successive differences as in Fig. 2.1). The third from the top is the  $d_3$  and the bottom the  $d_5$  detail coefficients. Note that the 4-km burst is not visible any more at the  $d_5$  level, after four successive averagings of the data. The top frame on the right is the  $a_{12}$  coefficients and below it  $d_7, d_9, d_{11}$ .

It is easily verified from the definitions above that the  $l^2$  norm of the data vector  $X$  can be written as

$$\sum_{n=1}^{2^M} (a_0(n))^2 = (a_M)^2 + \sum_{j=1}^M 2^{M-j} S_j, \quad (2.10)$$

which is another way of expressing the orthogonality of the decomposition of  $X$  into  $a_M$  and the  $d_j$ ,  $j = 1, \dots, M$ .

In Figure 2.5 we show log-log plots of scale spectra of nonoverlapping segments of the data, of length 655 m. Each plot contains scale spectra over 15 scales, from 4 cm to 655 m. Note that the scale spectra show a distinct departure from power law behavior for scales below one meter. On the longer scale side, power law behavior may be considered in the range of 2.5 m to 80 m, which corresponds to the detail coefficients  $d_7$  to  $d_{12}$ .

There are several important issues that must be addressed at this point, before we can continue with the scale spectral analysis.

- The temperature data are not a stationary time series. Therefore, computing scale spectra over long data segments that are not stationary, or approximately stationary, gives  $S_j$ 's that are hard to interpret and probably meaningless.
- The noise bursts in the data enter only in some of the detail coefficients, as can be seen from Figure 2.4. By restricting power law fitting to scale spectra from  $d_7$  to  $d_{12}$  we eliminate most of the noise.
- We want to fit a power law model to the scale spectra, like the ones shown in Figure 2.5, but even though the average slope of the log-log scale spectra over several segments is close to

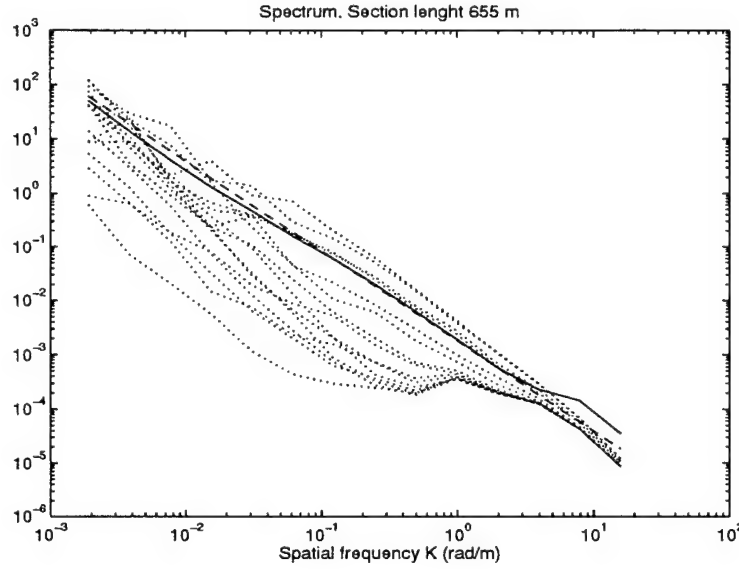


Figure 2.5: Scale spectra of 655 m nonoverlapping segments of the data ( $2^{15}$  points per segment) obtained from the Haar wavelet decomposition. The dashed line has slope  $-5/3$  as in Kolmogorov spectra. The solid line is the average over the scale spectra of the different segments. After the averaging is done the scale spectra are plotted in log-log format.

$-5/3$ , as the scaling theory of turbulence would predict, there is a lot of variability. A *local* power law model is likely to fit the data much better.

We must therefore deal with a larger class of models, local power law processes, and find effective ways to estimate them. We will base our analysis on two criteria. One is that the estimation of parameters should not depend on how the data are segmented. The second is that the variations of the slope and intercept for the log scale spectra must be on length scales that are much longer than those used to compute the spectra themselves. We will show with our analysis that both criteria can be met.

We begin by selecting four segmentations and estimating slopes and intercepts for the scale spectra obtained for each segment, as shown in Figure 2.6. The four segmentations are:

$$160m \ (2^{13} \text{ points}), 327 \ m \ (2^{14}), 655 \ m, (2^{15}), 1.31 \ km \ (2^{16}). \quad (2.11)$$

There are 512, 256, 128, 64 nonoverlapping segments, respectively, in each case. Within each segment we use only scale spectra from  $d_7$  to  $d_{12}$ , corresponding to length scales between 2.5 m and 80 m. We limit the longer scales to 80 m, well below the shortest segmentation length which is 160 m. We limit the shorter scales to 2.5 m because, as can be seen from Figure 2.5, below that scale the spectrum changes and power law fit is not appropriate. We return to the issue of selection of a range where the power law model is appropriate in Section 2.4.3. (Figures 2.28, 2.29, and 2.30). The fitting is done by least squares

$$\log S_j \approx \log C - p \log\left(\frac{2^j}{50}\right), \quad j = 7, 8, \dots, 12 \quad (2.12)$$

for each segment, and the units are adjusted so that the horizontal axis in Figure 2.6 is in kilometers.

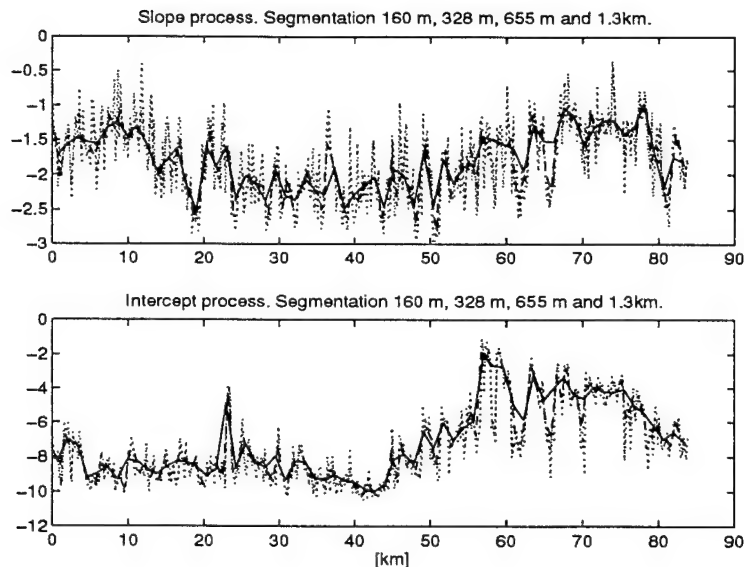


Figure 2.6: Top frame: slopes of log-log scale spectra from wavelet decompositions based on four different, segment lengths. At the finest resolution the scale spectra are calculated over nonoverlapping segments 160-m long. This is the dotted line that has the largest variations. At the next resolution the nonoverlapping segments are 327-m long (also plotted with a dotted line). The other two resolutions are 655m and 1.31 km and are shown with dashed and solid lines, respectively. The bottom frame is the same as the top, but now for the log intercept of the scale spectra.

We see from Figure 2.6 that the estimated slopes,  $p$ , and the log intercepts,  $\log C$ , vary considerably over the 80-km data set. They also depend on the segmentation, with the finer one having larger fluctuations (dotted lines). We must next develop a method for removing this dependence.

We can extract from the slope and log intercept process of Figure 2.6 the smooth, background variations. This can be done with a simple moving average or with a three-term matching pursuit [2] and the result is shown in Figure 2.7. Note that the smooth variations do not depend very much on the segmentation.

## 2.3 Filtering of the parameter processes

In this section we carry out a filtering of the slope and intercept processes of Figure 2.6, which approximately removes segmentation effects, that is, the dependence of the slope and intercept on the length of segment of the data that are used to estimate them. To motivate the filtering, we first simulate numerically temperature data with variable slope and intercept from Figure 2.7. This simulation replicates some important properties of the actual data. After the filtering, in Section 2.4, we will be able to generate more faithful simulations of the data.

### 2.3.1 Synthetic data

Stationary, Gaussian processes with power law spectra can be simulated efficiently by the method described fully in [3] and briefly in Appendix A. They can be simulated by frequency and time-domain methods as well. Local power law processes are, of course, not stationary since the slope and the log intercept vary. But they vary slowly, on the scale of hundreds of meters, compared to

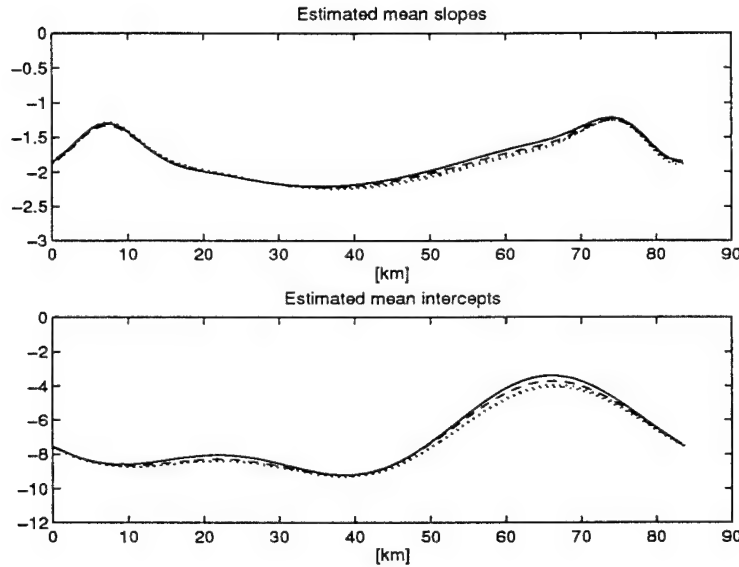


Figure 2.7: Top and bottom frames are smooth or background variations for the slope and intercept processes of Figure 2.6. The four lines correspond to the four different segmentations (resolutions). The two dotted lines correspond to the finer segmentations and the dashed and solid lines to the coarser ones, as in Figure 2.6.

the scale of 0.2 cm at which the process is sampled. In Figure 2.8 we show one realization of a local power law process simulated by varying the slope and log intercept according to Figure 2.7, discretized on a 1-km scale. The 84-km simulation shown contains  $2^{22}$  points.

The simulated temperature and temperature difference processes of Figure 2.8 do not look very much like the actual data of Figure 2.1. The simulations of Section 2.4 (Figure 2.18 and especially Figure 2.19, as well as Figure 2.31) are, however, much more faithful replications of the actual data, over the selected range of scales, as we explain below.

Even though the simulated temperature process does not look like the raw or actual data, the slope and log intercept processes that are obtained from it, for the four different segmentations (2.11) we used for the actual data, are quite reasonable, as can be seen from Figure 2.9. The fluctuations of the estimated slope and log intercept are smaller than the ones for the actual data in Figure 2.6. This is to be expected since we used only the smooth background of the actual slope and log intercept, Figure 2.7, in the simulations. What is important, however, is dependence on the segmentation. The sensitivity of the estimated slope and intercept processes to the segmentation corresponds roughly to that seen for the actual data.

We can now state more precisely our basic strategy for removing dependence on segmentation and identifying accurately the structure of the temperature process. We will assume that it is a *two-scale local power law* process. This means that it is a Gaussian process with power law spectrum for which the slope and log intercept themselves are stochastic processes that vary slowly relative to the underlying one. We will assume, moreover, that the slow modulation processes that characterize the slope and log intercept are statistically independent of the power law process.

We will use the variogram, or structure function, to estimate statistics of the slope and log intercept processes. For a time series  $\mathbf{Y} = (Y_i)$  of size  $N$  the empirical variogram with lag  $j$  is

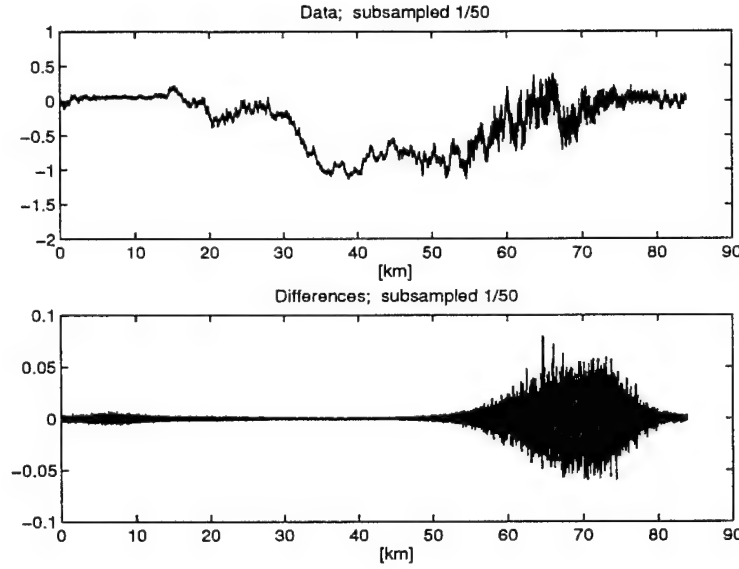


Figure 2.8: Simulation of an 84 km segment of the temperature process as a Gaussian, local power law process with slowly varying slope and intercept as obtained from the actual data and shown in Figure 2.7. The simulation is done with the algorithm described in Appendix A. The top frame is the simulated temperature and the bottom its successive differences.

defined by

$$V(j) = \frac{1}{2(N-j)} \sum_{k=1}^{N-j} (Y_{k+j} - Y_k)^2 \quad (2.13)$$

with dependance on the length of the data vector  $N$  not shown. In Figure 2.10 we show the variograms for the *fluctuations* of the slope and log intercept process of the simulated data. That is, the difference between the curves in Figure 2.9 and the background in Figure 2.7. On the left in Figure 2.10 we use the processes obtained with the finest segmentation (160 m) and on the right with the next coarser (327 m). It is clear that the variograms are essentially flat, which indicates that the estimated slope and intercept processes have trivial correlation structure (white noise). This is not the case with the *actual* data, as we will see in the next section.

In Figure 2.11 we show Fourier spectra for the fluctuations of the slope and intercept processes of the simulated data. The spectra are very fluctuating but have no particular structure, supporting thus the white noise behavior that was suggested by the variograms in Figure 2.10.

### 2.3.2 Measured data

For the actual data the estimated slope and log intercept processes are shown in Figure 2.6, for each of the four segmentations. The variograms for these processes are shown in Figure 2.12 for the finest segmentation, and in Figure 2.13 for the coarsest. They clearly have more structure than their analog for the simulated data in Figure 2.10. There are three important parameters that emerge, and are estimated, from the variograms of Figure 2.12 that we shall use: the vertical intercept, the level of the horizontal asymptote, and the decay rate of the exponential curve that is fitted to the points obtained from the data. For the finest segmentation (160 m each, 512 of them) the estimated parameters are as follows:



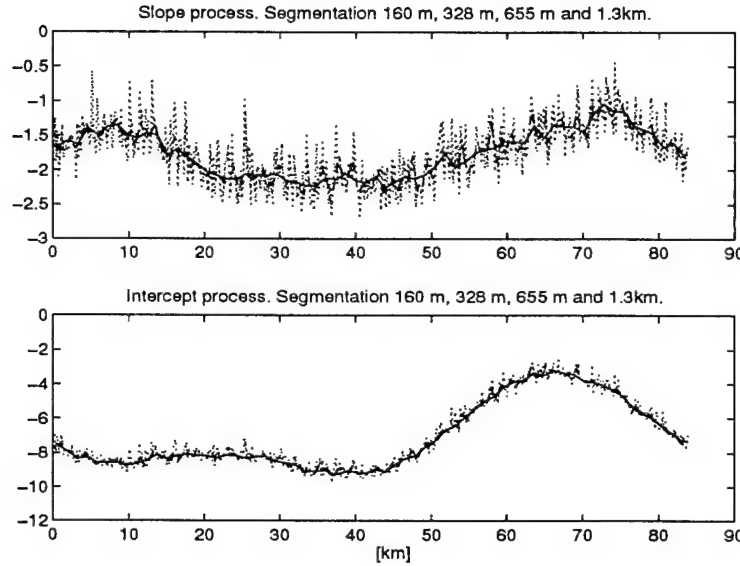


Figure 2.9: Slope (top frame) and log intercept (bottom frame) processes obtained from the simulated temperature data shown in Figure 2.8. The four curves, two dotted, one dashed and one solid, correspond to slopes and log intercepts obtained from scale spectra with segments of four different lengths, as was done for the actual data and shown in Figure 2.6. The smooth background of these processes coincides with the one we used in the simulations (Figure 2.7). The fluctuations about the background are not as large as the ones for the actual data, shown in Figure 2.6.

- **For the slope:** Vertical intercept  $\sigma_n^2 = 0.09$ , horizontal asymptote level  $\sigma_n^2 + \sigma_s^2 = 0.21$ , and correlation length 640 m (four segment lengths).
- **For the log intercept:** Vertical intercept  $\sigma_n^2 = 0.13$ , horizontal asymptote level  $\sigma_n^2 + \sigma_s^2 = 1.83$ , and correlation length 480 m (three segment lengths).

The vertical intercept can be used to identify a white noise component  $\sigma_n^2$  in the estimated slope and log intercept processes. The exponential and the asymptote level can be used to identify the intrinsic variation of the parameters; we model this process component as being stationary after the background is subtracted out. We also assume that the white noise and the exponentially correlated fluctuation processes are independent. This is a reasonable hypothesis because of the separation of scales in the two-scale power law model that we take as modeling the temperature data. In the next section we use the information we have gotten from the variogram to introduce a model for the slope and intercept process of Figure 2.6 and then to filter them so as to remove the effects of segmentation.

### 2.3.3 Filtering of the slope and log intercept processes

We now model the slope and log intercept processes by a white noise process plus one with known background and covariance and then filter out the white noise. Filtering out the white noise component of the estimated processes obtained from the actual data will give us the *intrinsic* slope and intercept processes that *should not depend on the segmentation*. This is what we do in this section. The slope and intercept processes for the actual data are shown before the filtering in Figure 2.6 and *after* the filtering in Figure 2.14. Note that after the filtering all four segmentations

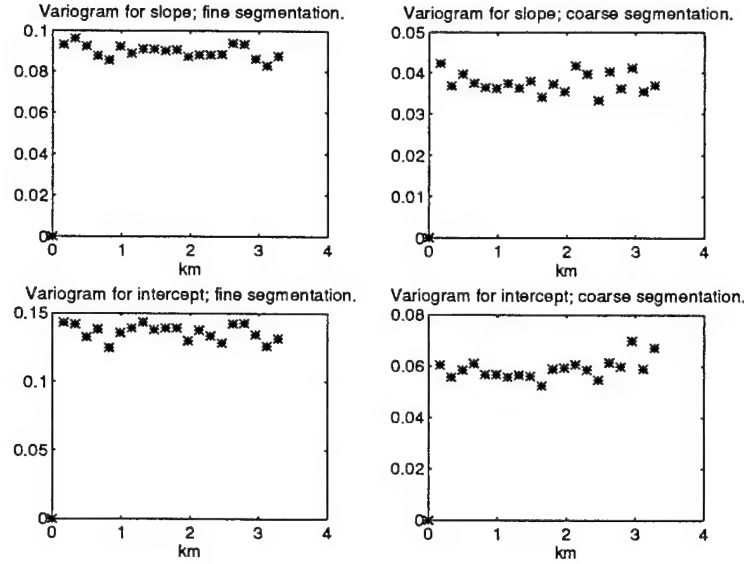


Figure 2.10: Variograms for the fluctuations of the estimated slope and log intercept processes of the scale spectra of the simulated temperature data at the two finest segmentations (left frames are for the the finest segmentation). Note that the variograms are flat, which indicates that the fluctuations of the slope and log intercept processes are essentially white.

give essentially the same result, the solid curve in Figure 2.14. This is a very strong indication that the model we have chosen and the analysis that we have followed fit the aerothermal data very well. Recall, however, that the correlation length of the slope and log intercept processes were approximately 500 m. Therefore, when the parameters are estimated based on the two coarsest segmentations (655 m and 1.3 km), the parameter processes are smoothed somewhat and the estimates do not faithfully represent their variability. This is verified by Figure 2.14, since the two dotted curves, corresponding to the coarser resolutions, are somewhat smoothed versions of the solid line that corresponds to the two finest resolutions. In Figures 2.15 and 2.16 we show explicitly the action of the filters. Figure 2.15 corresponds to the slope parameter and Figure 2.16 to the log intercept process. The four frames in the figures correspond to the different segmentations with the finest at the top. The dotted lines are the estimated parameters before filtering and the solid lines after filtering. Note that for the two finest resolutions the variability of the parameters are captured, but the sampling noise is large. The sampling noise is, however, removed by the filtering. For the two coarsest resolutions the parameter processes are overly smoothed. Figure 2.17 is a scatterplot of the filtered slope and log intercept processes. It shows that there is positive correlation between them, a fact that has some physical basis.

The filtering is done as follows. Let  $\mathbf{Y} = (Y_i)$ ,  $i = 1, \dots, N$  be the observed slope or intercept process obtained with a fixed segmentation. We model it by a process of the form

$$Y_i = S_i + n_i = \bar{S}_i + S'_i + n_i, \quad i = 1, \dots, N \quad (2.14)$$

where  $\bar{S} = (\bar{S}_i)$  is the background, which we model as deterministic,  $S' = (S'_i)$  is the fluctuation about the background, taken to be a stationary stochastic process with exponential correlation, and  $\mathbf{n} = (n_i)$  is a white noise process with fixed noise level. The three parameters needed in the modeling are provided by the variogram analysis of the previous section. We estimate the

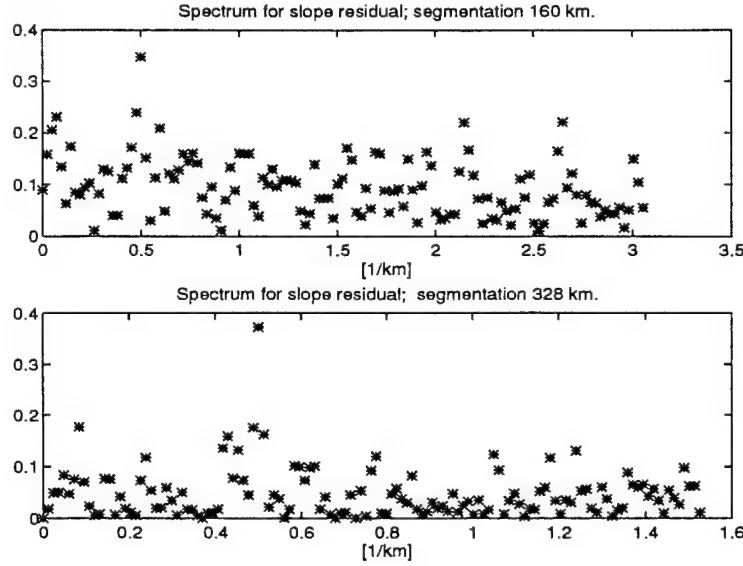


Figure 2.11: Fourier spectra of the fluctuations of the slope of the scale spectra of the simulated temperature data. The top frame is for the finest segmentation and is computed by averaging the Fourier spectra of the two halves of the slope process, each containing 256 points. The bottom frame is for the next-to-the-finest segmentation and is a single Fourier spectrum for the slope process with 256 points. The spectra are very fluctuating but do not have distinguishing features.

background  $\bar{S}$  by the smooth curves shown in Figure 2.7.

We now construct a filter (matrix)  $\Lambda$  that transforms the data  $\mathbf{Y}$  to  $\Lambda\mathbf{Y}$  in such a way that

$$E\{\|\Lambda\mathbf{Y} - \mathbf{S}\|^2\} \quad (2.15)$$

is minimized over all matrices  $\Lambda$  that also preserve the mean of  $\bar{S}$  of  $\mathbf{S}$ , that is  $\Lambda\bar{S} = \bar{S}$ . If  $\sigma_n^2$  is the white noise level and  $C_s$  is the covariance matrix of  $\mathbf{S}'$ , then

$$\Lambda = (C_s + \sigma_n^2 I)^{-1} [C_s + \mathbf{v}^T \otimes \bar{S}] \quad (2.16)$$

where the vector  $\mathbf{v} = (v_i)$  is given by

$$v_i = \frac{\bar{S}_i - \bar{S}^T (C_s + \sigma_n^2 I)^{-1} C_{s,i}}{\bar{S}^T (C_s + \sigma_n^2 I)^{-1} \bar{S}}. \quad (2.17)$$

Here  $C_{s,i}$  is the  $i^{th}$  column of the matrix  $C_s$  and the superscript  $T$  stands for transpose. Filtering of this kind is discussed in [4].

## 2.4 Simulated data based on the filtered slope and log intercept processes

### 2.4.1 Replication with filtered slope and log intercept

The filtered slope and log intercept processes shown in Figure 2.14 (solid line) essentially do not depend on the segmentation and are, therefore, intrinsic to the temperature data. We can now simulate this data as a Gaussian, local power law process with slope and log intercept varying

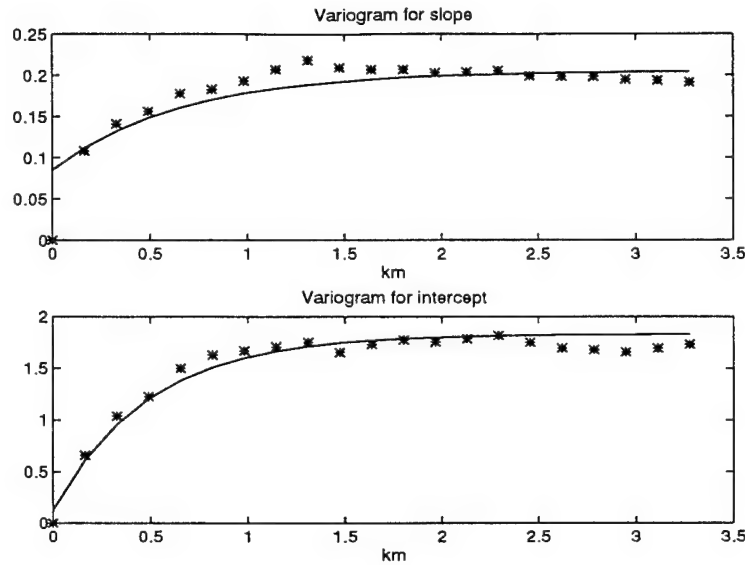


Figure 2.12: Variograms for the fluctuations, relative to their smooth background shown in Figure 2.7, of the slope (top) and log intercept (bottom) processes of the scale spectra of the *actual* data, obtained with the finest segmentation (Figure 2.6). The stars are computed points and the solid curve a fitted exponential with a level asymptote. The important parameters obtained from the fitting are the vertical intercept (white noise component), the decay rate (correlation length), and the level of the asymptote (variance of the fluctuations).

according to Figure 2.14. We discuss the issue of how to best simulate the temperature data in Appendix A.

A simulation of the temperature data done this way is shown in Figure 2.18. This should be contrasted to the simulation of Figure 2.8 where only the background, Figure 2.7, of the slope and intercept process is used. Figures 2.1 and 2.18 have common features, like a more energetic second half (in the region of 53 to 83 km).

A more striking similarity between the actual and the simulated data emerges when they are both filtered so that only scales  $d_7 - d_{12}$  contribute. This corresponds to the length scales in the range 2.5 to 80 m that we use in estimating slopes and log intercepts of the power law. Figure 2.19 shows the results and they are, indeed, striking. In Figure 2.20 we illustrate that the simulation replicates the data faithfully only for the targeted scales. The top plot shows the reconstruction of the actual data from  $d_1$  to  $d_7$  only and is very different from the corresponding reconstruction for the simulated data, middle frame. Note also that the reconstruction of the actual data from  $a_{12}$  only is very different from the corresponding reconstruction of the simulated data, as can be seen from Figure 2.20, bottom frame.

We can now treat the simulated temperature data of Figure 2.18 as we did with the actual data. In Figure 2.21 we show the slope and log intercept processes obtained with the four different segmentations of (2.11). These curves appear to be very similar to the ones for the actual data, Figure 2.6, but there are important differences. When we compute the variogram of the fluctuations of the slope and log intercept processes, the analog of Figure 2.12, we get Figure 2.22.

The stars in Figure 2.22 correspond to the variogram obtained when the slope and log intercept used to generate the simulation (Figure 2.14) are subtracted from the corresponding processes

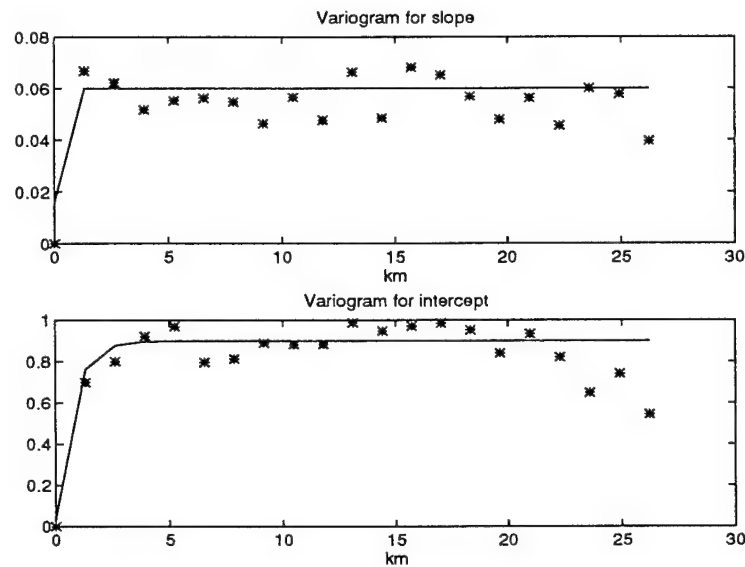


Figure 2.13: Same as Figure 2.12 but with the slope and log intercept process obtained from the coarsest segmentation.

estimated from the simulation. This gives the variogram of the sampling error. Note that the flatness and level of the star curves in Figures 2.10 and 2.22 are close to each other, for the finest resolution. The crosses in Figure 2.22 correspond to the variogram of the filtered slope and log intercept when only the smooth background is subtracted out. The solid line is as in Figure 2.12, which is the model variogram for the sampled slope and log intercept processes from the real data. Note that the crosses are located somewhat below this line. The reason for this is that the filtering of the sampled slope and log intercept, which approximately removes the sampling error, reduces somewhat the variability in the slope and log intercept processes. This is seen from Figure 2.23, where we replot the crosses, and the stars now correspond to the variogram of the slope and log intercept processes used in the simulation, which are given by Figure 2.14.

We see that only the white noise component persists (the flat lines). The solid curves in Figure 2.22 are the ones from the actual data of Figure 2.12. In Section 2.4.4 we show how to generate simulated data that replicate the actual variograms. The reason we do not get this now is because we have treated the filtered slope and log intercept curves of Figure 2.14 as *deterministic* curves, rather than realizations of a stochastic process with the structure of Section 2.3.3.

When we now filter the simulated slope and log intercept processes of Figure 2.21 to remove the white noise part, as we did in Section 2.3.3, we get the curves in Figure 2.24. These curves are, again, essentially independent of the segmentation and differ very little from the ones in Figure 2.14, which we got from the actual data, as can be seen from Figure 2.25. We have, therefore, recovered faithfully from the simulated data the information that we used to generate it.

## 2.4.2 Sampling error

The slope and log intercept processes are obtained from the temperature data and are, therefore, functionals of one realization of a stochastic process. How much sampling error is there in the curves of Figure 2.14? Stated in another way, if we generate several independent realizations of the temperature data that replicate faithfully its local-power-law-based statistical properties, how much

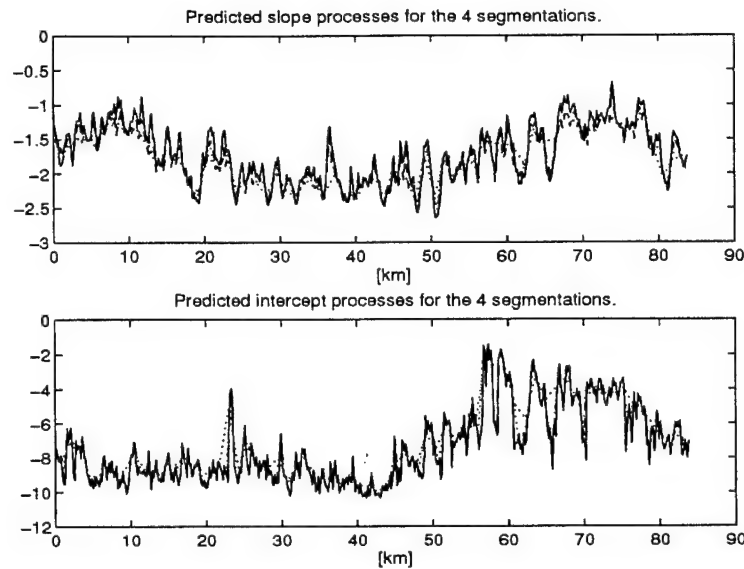


Figure 2.14: Filtered slope (top) and log intercept (bottom) processes of the actual data for the four different segmentations. Note that all four segmentations of the filtered processes are essentially the same. The solid and dashed lines correspond now to the two finest resolutions and are indistinguishable. The dotted curves correspond to the two coarsest segmentations and are slightly smoother versions of the other curves. The filtering has eliminated the differences in the slope and log intercept processes that are due to the segmentation (as in Figure 2.6). It has also eliminated the white noise component of the slope and log intercept fluctuations that is due to sampling. The effect of sampling alone is seen from the simulated slope and log intercept process in Figure 2.9.

variation will we see in the slope and log intercept processes from realization to realization? This is the bootstrap way of estimating error. When we do this with twenty independent simulations of the temperature data, like the one of Figure 2.18, we get Figure 2.27, where the mean and two standard deviations about it are shown (making the mean curve darker). The sampling standard deviation should be close to the noise level  $\sigma_n$  that we got from the variogram analysis in Section 2.3.2 and that we used in the filtering in Section 2.3.3. This is in fact the case for the log intercept process error but not for the slope error, which is smaller than what we got from the variogram analysis. This can be explained by looking more carefully at the bias error in the slope in Figure 2.25.

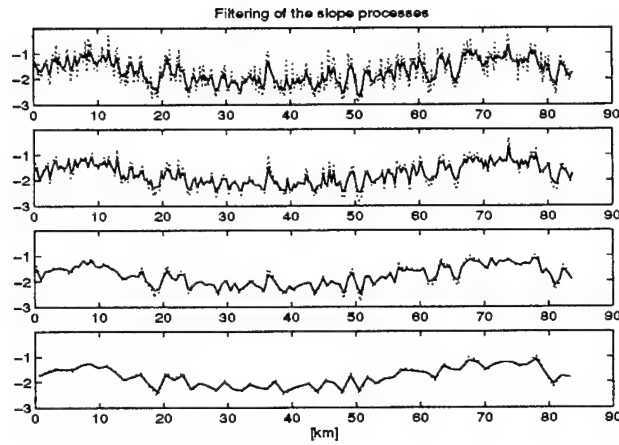


Figure 2.15: Filtered (solid) and unfiltered (dotted) slopes for the four segmentations, with the finest (160 m) at the top.

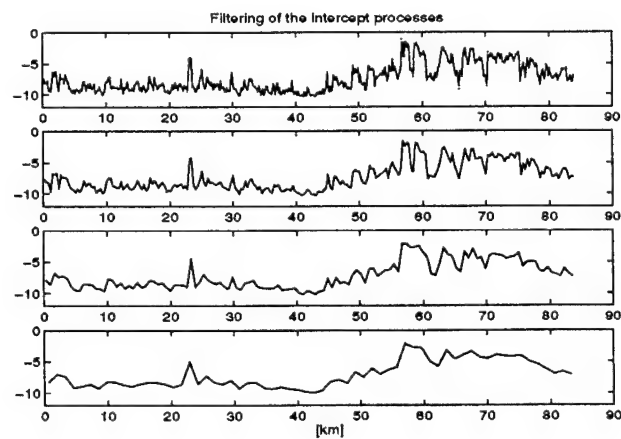


Figure 2.16: Same as Figure 2.15 but for intercepts.

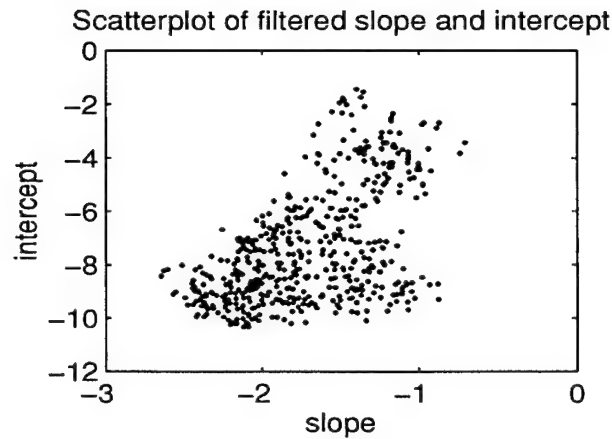


Figure 2.17: Scatterplot of the filtered slope process versus the filtered log intercept process for the actual data (Figure 2.14). Note the positive correlation between the slope and the log intercept.

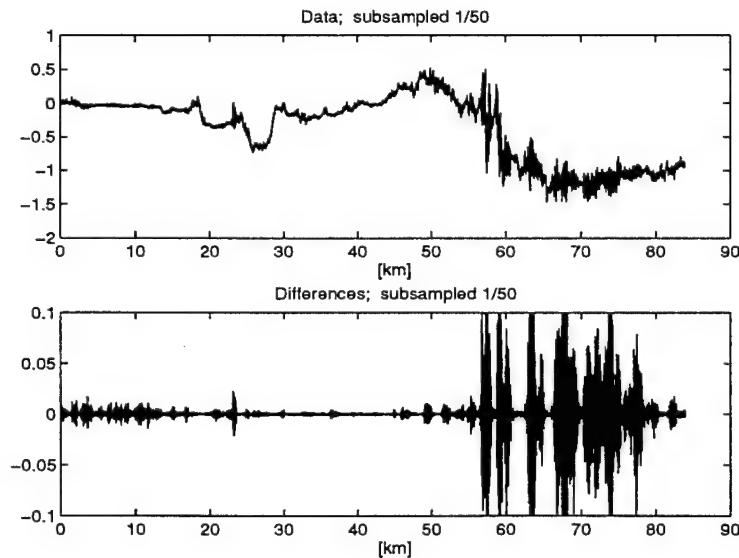


Figure 2.18: Simulated temperature (top) and temperature differences (bottom) by a Gaussian, local power law process with slope and log intercept obtained from the actual data and shown in Figure 2.14 (solid line). If only the background (Figure 2.7) is used the simulation is shown in Figure 2.8. The differences between the two simulations are more apparent in the temperature differences (the bottom frame here and in Figure 2.8).



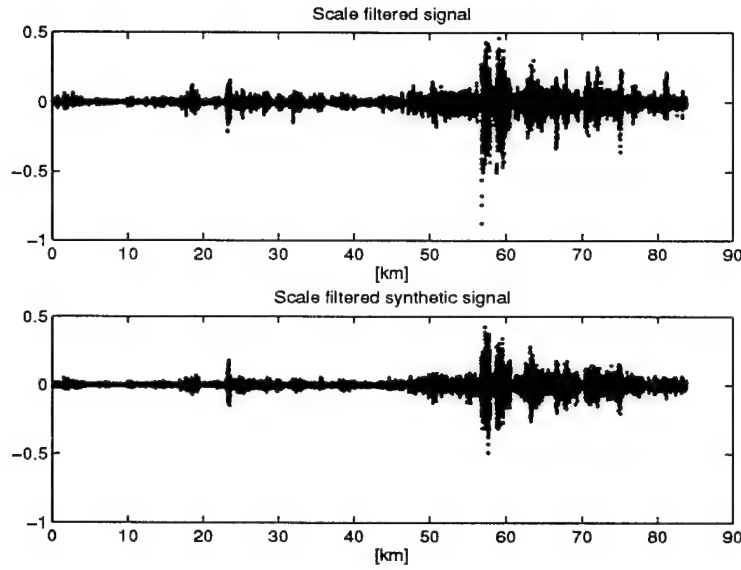


Figure 2.19: The *actual* temperature data set (top frame) obtained by synthesizing it from the detail coefficients  $d_7 - d_{12}$  of its Haar decomposition. It is information from this range of scales that enters into the slope and intercept processes. The bottom frame is the same as the top but for the *simulated* data of Figure 2.18. Note the striking similarity between the two figures.

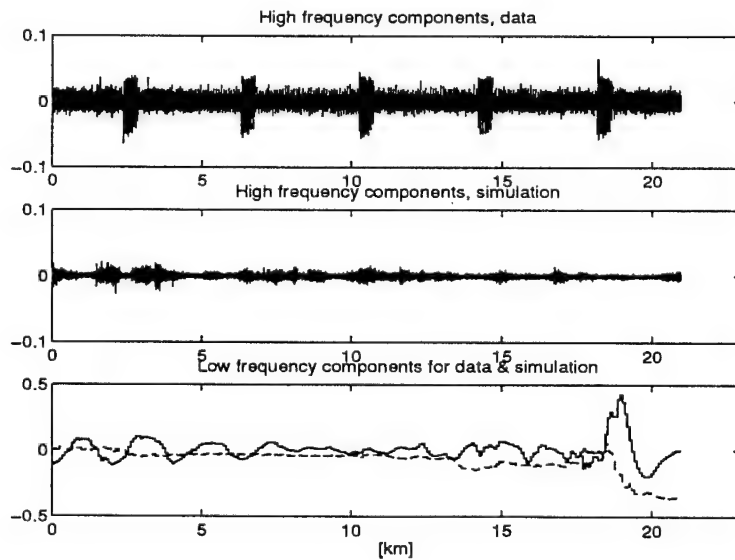


Figure 2.20: The temperature data reconstructed with only the  $d_1 - d_5$  coefficients (top frame). The middle figure is the same as the top but for the *simulated* data of Figure 2.18. Note the dissimilarity between the two figures. The bottom frame is temperature data reconstructed with only  $a_{12}$ , for the actual data (solid) and the simulated data (dashed).

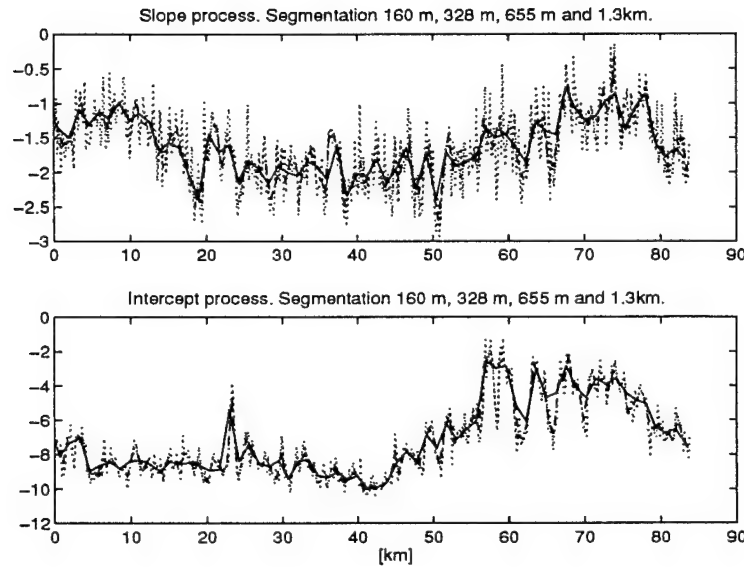


Figure 2.21: Slope (top) and log intercept (bottom) processes for scale spectra of the simulated process of Figure 2.18, with four different segmentations, as with the actual data and shown in Figure 2.6. The Figure above and Figure 2.6 are quite similar.

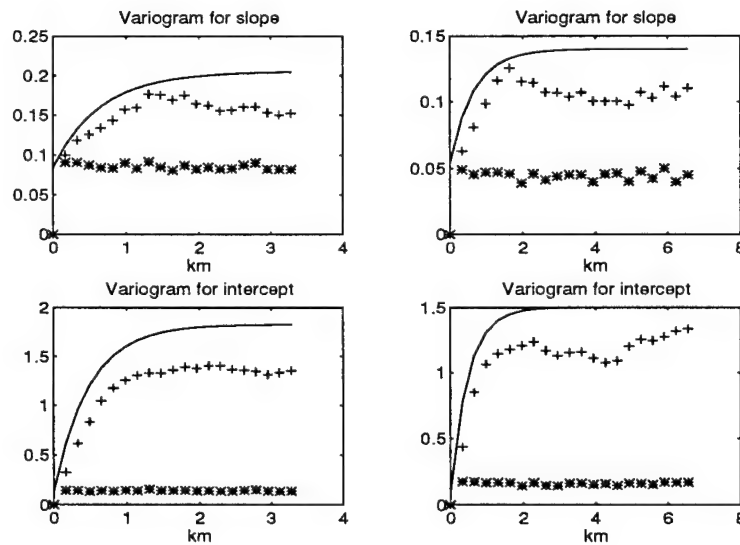


Figure 2.22: Variograms for the fluctuations of the slope (top) and log intercept (bottom) processes obtained from the simulated temperature data shown in Figure 2.18. The stars are computed from the fluctuations when the filtered background is subtracted. The solid curves are exactly the ones fitted to the *actual* data and shown in Figure 2.12. The crosses are variograms for fluctuations when only the smooth background (Figure 2.7) is subtracted. The curves on the left are from data at the finest, 160 m, resolution while those on the right are for the next to finest, 330 m.

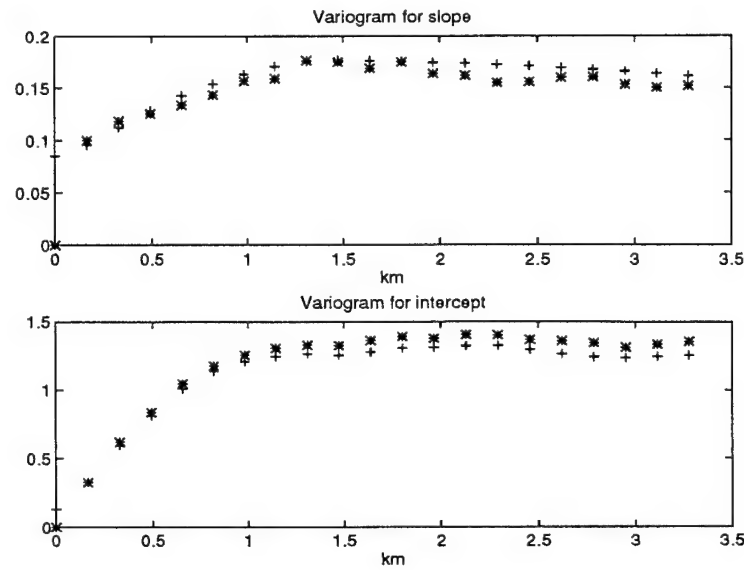


Figure 2.23: The crosses are as in Figure 2.22 and the stars are the empirical variogram of the actual data that are used in the simulation, that is, variograms for the slope and intercept of Figure 2.14 after filtering.

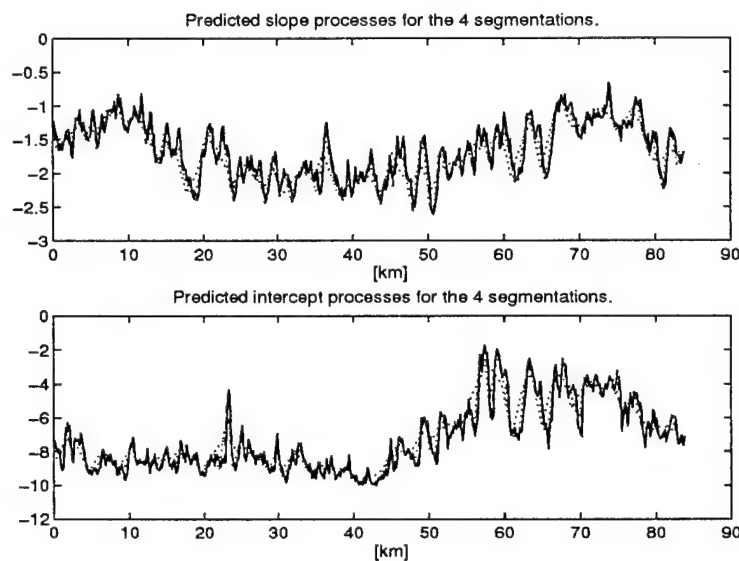


Figure 2.24: Filtered slope (top) and log intercept (bottom) processes from the scale spectra of the *simulated* temperature shown in Figure 2.18. The different curves correspond to the different segmentations, as in Figure 2.14 for the *actual* data. The similarity between the curves above and the ones in Figure 2.14 show that the simulations replicate faithfully the information from the actual data that is used in generating the simulated data.

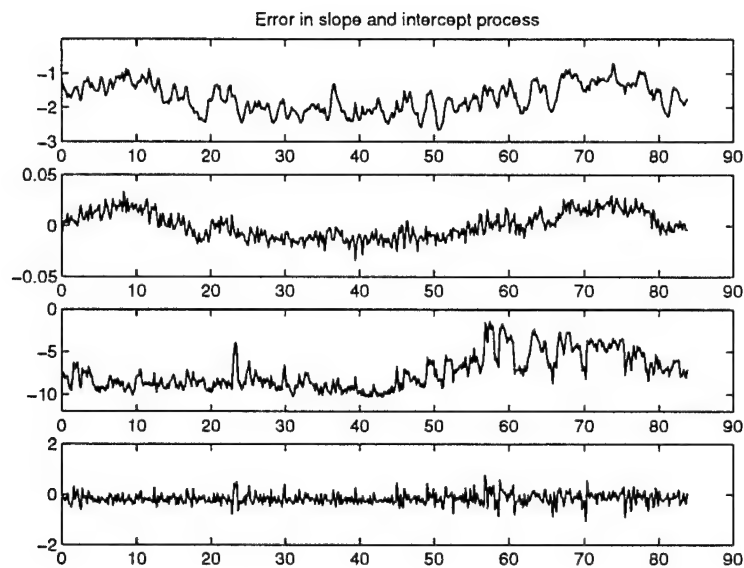


Figure 2.25: The top frame shows two curves, the slope process for the actual data (Figure 2.14, top) and the slope process for the simulated data (Figure 2.24, top). The second figure from the top is the difference between these two curves. Note the slight bias in the otherwise small error. The bottom two frames are the same as the top two but for the log intercept process.

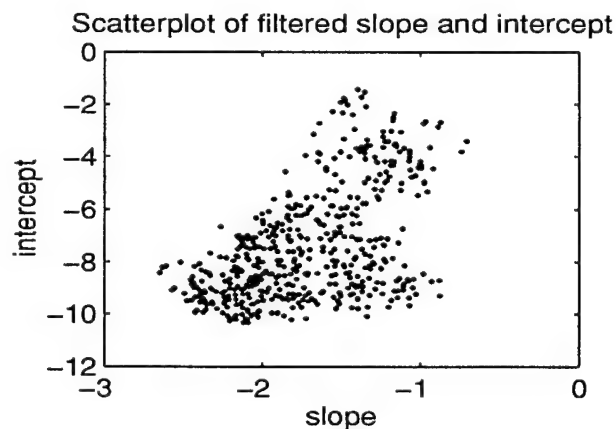


Figure 2.26: Scatterplot for the filtered slope and intercept process of Figure 2.24 (simulated data).

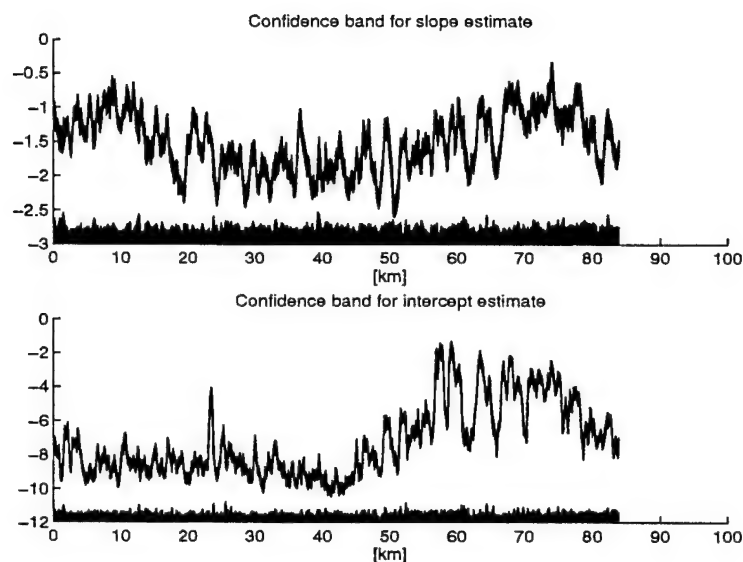


Figure 2.27: Mean over twenty independently simulated filtered slope (top) and log intercept (bottom) processes. Each simulation of the temperature data is like the one of Figure 2.18. Each filtered slope and log intercept process is like Figure 2.24. Twice the pointwise standard deviation is shown (to scale) just above the horizontal axis of each figure. The two-standard-deviation band is also superimposed on the mean values of the slope and intercept, making them appear darker.

### 2.4.3 Error in parametric fitting of scale spectrum

We explained in Section 2.2, below (2.11), that the slopes and log intercepts are obtained by fitting the log scale spectra from  $d_7$  to  $d_{12}$  to a line, in each segment. How good is this fit and, more important, could we have done better with a wider or a narrower range of scale spectra? We measure the error in the fit by the sum of the squares of the differences of the log spectra from the fitted line. For each segment we then divide this error by the average over the different segments of the corresponding error for the *simulated* temperature data. This is shown in the top Figure 2.28. If for the *simulated* data we replace the numerator by the error in the fit in each segment, we then get the bottom frame in Figure 2.28. The fact that the top and bottom frames in this Figure are comparable shows that the model is appropriate over the considered scales. That is, the misfit in the actual data (top frame) is comparable to the one for simulated data, which is the most we can expect.

In Figure 2.29 we show what happens when we use two additional small scale spectra in the fit. This takes us to the right of the change point (at about 60 cm) in Figure 2.5 so we expect a worse fit. This is in fact what Figure 2.29 shows, since the relative error for the actual data (top frame) is substantially bigger than the simulated (reference) relative error (bottom frame).

The situation is similar if we use only the smooth background (Figure 2.7) and calculate the fit in each segment with values from it. We then divide this error with the corresponding one for the simulated data where only the smooth background is used (Figure 2.8). We see that for the actual data the relative error (top frame) is substantially bigger than the relative error for the simulated data, the reference error (bottom frame). Hence, a local power law model is not a good model when we consider these extended sets of scales.

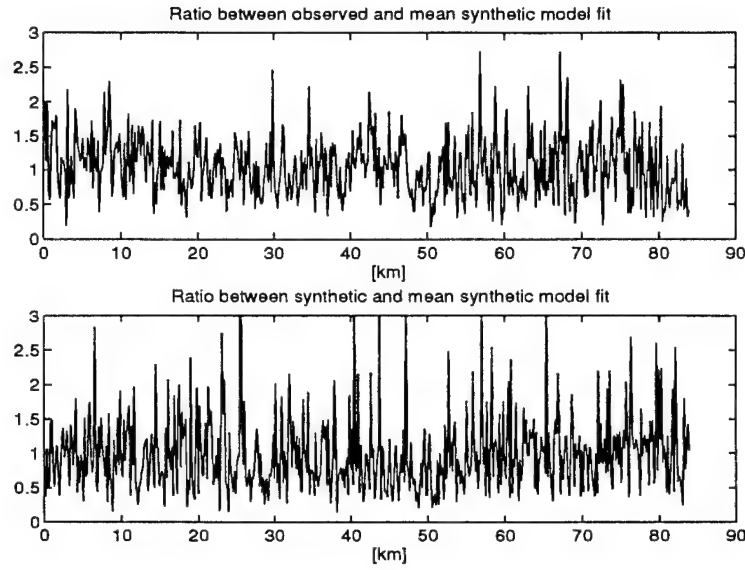


Figure 2.28: Top: The ratio of the  $l^2$  norm of the difference between the log-log scale spectrum and the power-law fitted log-log spectrum for the *actual* data (finest segmentation,  $2^{13}$  points each) over the mean (over the 512 segments) of the  $l^2$  norm of the difference between the scale spectrum and the power-law fitted spectrum for the *simulated* data. Bottom: Same as for the top frame with only simulated data. The scale spectrum corresponding to  $d_7$  to  $d_{12}$  is used in calculating the  $l^2$  error and in the power law fit. This contains information in the data over length scales of 2.5 m to 80 m.

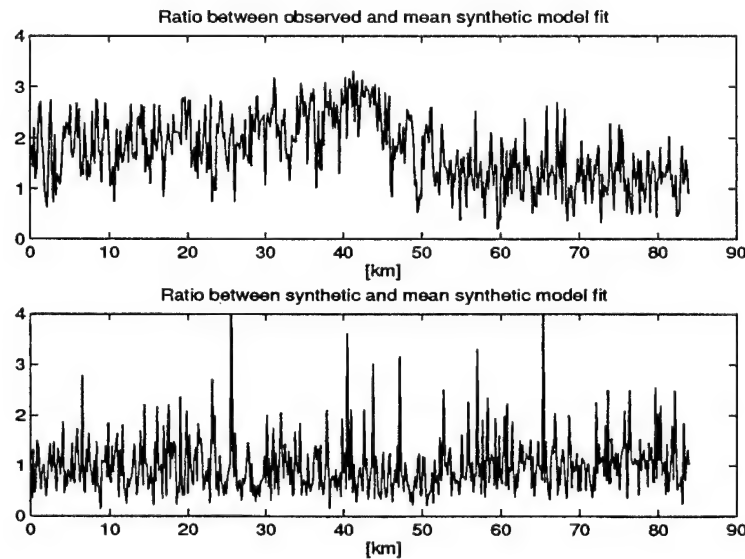


Figure 2.29: Same as Figure 2.28 except that two additional scale spectral points are used, corresponding to  $d_6$  and  $d_5$ . This contains information in the 0.6 m to 80 m range.

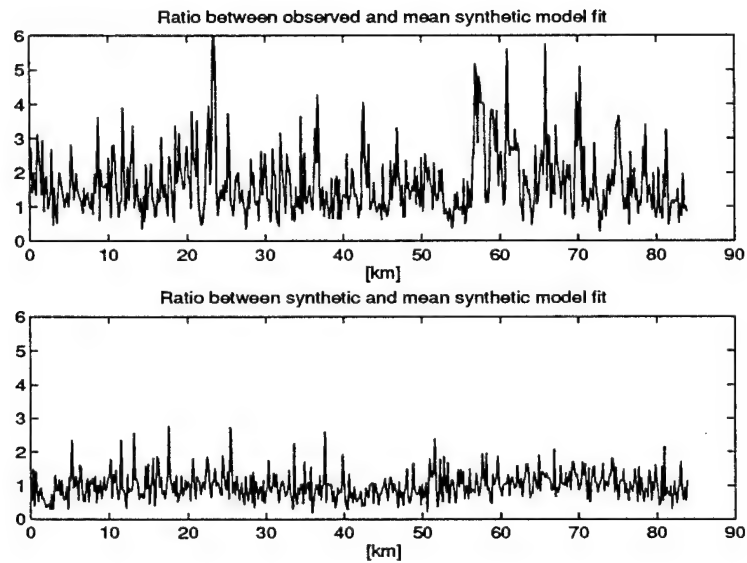


Figure 2.30: Same as in Figure 2.28 except that the simulations are based on the smooth background, as in Figure 2.7, and the residual is also computed relative to the smooth background. Note that the relative error for the actual data (top frame) is considerably larger than the corresponding one for the simulated data (bottom frame). This should be contrasted with Figure 2.28 where the two error ratios are comparable.



#### 2.4.4 Replication with random slope and log intercept

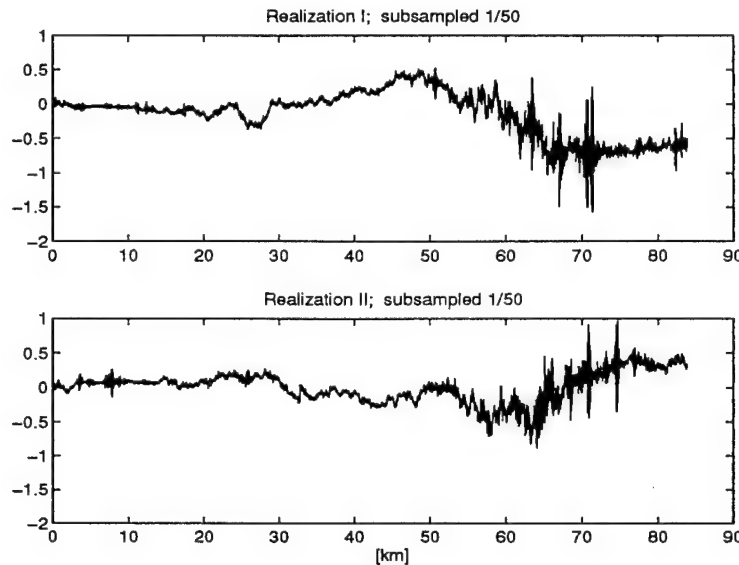


Figure 2.31: Two different realizations of simulated temperature data (top and bottom frames) in which the slope and log intercept are Gaussian stochastic processes with mean as in Figure 2.7 and fluctuations determined by the variogram analysis of Section 2.3.2. The slope and the log intercept fluctuations are generated from the same white noise sequence that is independent of the power law process.

The replication of the temperature data as a local power law process with slowly varying, *deterministic* slope and log intercept is done in Section 2.4.1. The filtered slope and log intercept of Figure 2.14 are used and a typical realization is shown in Figure 2.18. Simulations of this sort are much more faithful than the ones based only on the smooth background of Figure 2.7, and shown in Figure 2.8. However, even though the simulations of Section 2.4.1 replicate well the input slope and log intercept, as seen from Figure 2.25, the output slope and log intercept of Figure 2.24 do not have the right correlation structure. This is clear from the variogram analysis of the simulated slope and log intercept fluctuations shown in Figure 2.22. The filtering of the processes removes some of the intrinsic variability of the parameter processes, which puts the crosses considerably below the solid lines.

How can we generate realizations of temperature data that produce slope and log intercept processes with a variability like the ones for the actual data in Figure 2.12? To this effect, we let the slope and log intercept be themselves stochastic processes that have the form (2.14), with the background  $\bar{S}$  given as in Figure 2.7, fluctuations about the background  $S'$  taken to be stationary, Gaussian stochastic processes with exponential covariance as estimated in Section 2.3.2, and without the white noise term  $n$ . The fluctuation processes for the slope and log intercept are generated from the same white noise sequence, which we take to be independent of the underlying power law process. This is a crucial assumption that can be justified by the wide separation scales between variations of the basic power law process (centimeters to tens of meters) and those of its slope and log intercept (hundreds of meters to kilometers). We use the same white noise sequence to generate both the slope and log intercept, since we expect these processes to be strongly correlated.

Simulated temperature data with random slope and log intercept are shown in Figure 2.31.

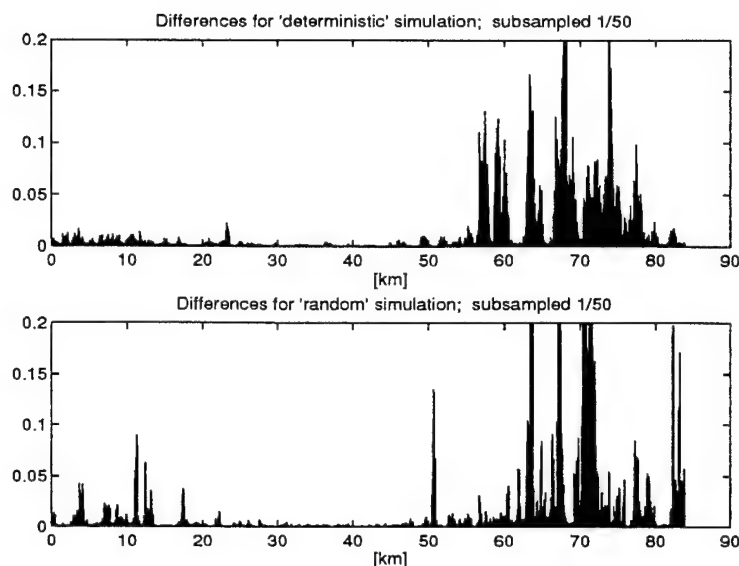


Figure 2.32: Absolute values of temperature differences for the simulation of Figure 2.18 with deterministic slope and intercept (top frame) and for the top of Figure 2.31 (bottom frame).

Comparison with Figure 2.18, which is simulated data that has deterministic slope and log intercept, shows that the two data sets are qualitatively similar but the fluctuations in the differences are bigger for the random case, as can be seen from Figure 2.32 where we plot the absolute value of temperature differences for the case of deterministic slope and log intercept (top frame) and the random case (bottom frame). The estimated slope and log intercept for the simulation of Figure 2.31, for the four segmentations (2.11), is shown in Figure 2.33. The variograms of the fluctuations of the slope and log interface of Figure 2.33 are shown in Figure 2.34 (stars). We see from this figure that the estimations are slightly biased, which is not surprising since complex nonlinear transformations are involved. The scatterplot for the estimated slope and log intercept is shown in Figure 2.36 and it does indicate positive correlation as in Figure 2.17. The filtered slope and log intercept processes are shown in Figure 2.35. From Figure 2.24 we see that the fluctuations in the slope are comparable in the two simulations, while the fluctuations of the log intercepts are stronger for the 'random' case of Figure 2.31.

It is clear that when the input slope and log interface in the simulation of a local power law process are themselves random, we do not get estimated slopes and log intercepts that replicate pointwise the actual ones. So we should not expect a close match between Figures 2.14 and 2.35, as we have between Figure 2.14 and 2.24 (see Figure 2.37). We do, however, get a close match (up to a small bias) of the variograms of their fluctuations, the stars and crosses in Figure 2.34. So the statistics of the slope and log intercept are now well replicated.

#### 2.4.5 Intrinsic variability of the slope and log intercept process

Let us also look at the standard deviation of the parameter estimates by generating several (twenty) independent realizations, as in the previous section, and then estimating and filtering the slope and log intercept processes. As shown in Figure 2.38 the two-standard-deviation band is nearly twice as big as that obtained with simulations that have 'deterministic' parameters, as in Figure 2.27.

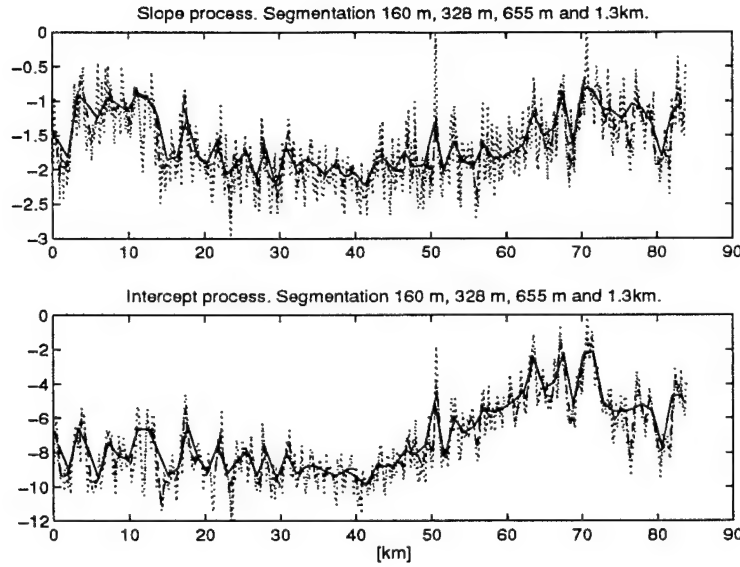


Figure 2.33: Slope (top) and log intercept (bottom) processes estimated for the four basic segmentations (2.11) from the simulated data of Figure 2.31.

## 2.5 Summary and conclusions

The main premise driving our analysis of temperature data from a turbulent atmosphere is that it is a local power law process. This means that the power law itself—the power (slope) and the multiplicative constant (log intercept)—is not a constant but a slowly varying function, deterministic or random. We estimate the slope and log intercept of the scale spectrum by appropriately segmenting the data and then removing segmentation effects by a filtering process. When a local power law process is simulated with the parameters estimated from the data, we get a faithful replication of its basic statistical properties. The replication is sample-wise faithful but statistically inaccurate when the slow variation is deterministic (Section 2.4.1). The simulation is sample-wise distinct from the actual data when the slope and log intercept are taken as random in the simulation, but the statistics are faithfully reproduced (Section 2.4.4). This and the removal of segmentation effects are a very strong indication that the model and the analysis that we have followed capture the essential features of the data.

An important aspect of the model that we use is separation of scales in the variation of the estimated parameters (slope and log intercept) from the underlying process that generates the power law spectra. This will be the starting point for a detailed theoretical development of the methods that we have introduced here.

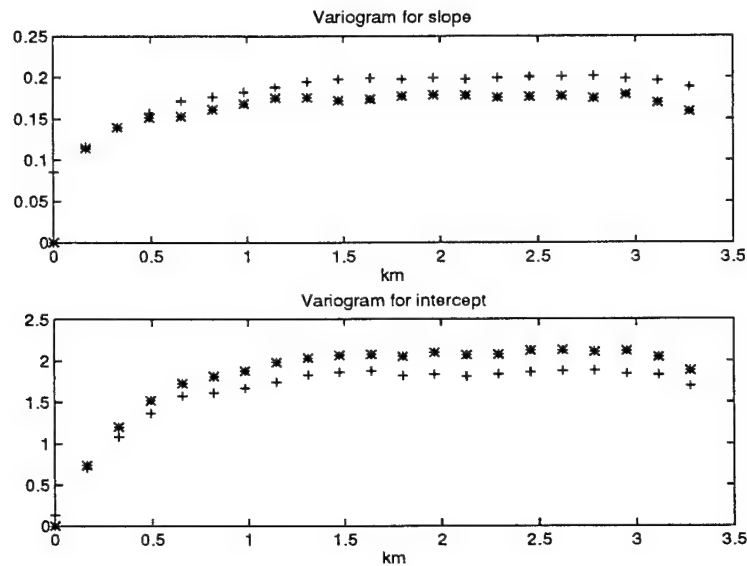


Figure 2.34: Variograms for the slope and intercept fluctuations from Figure 2.33, with the finest resolution. The stars are from the simulated data and the crosses from the actual data of Figure 2.12. Note that the horizontal asymptote for the slope is under-estimated while the one for the log intercept is over-estimated. This is due to a small bias in the nonlinear estimation procedure.

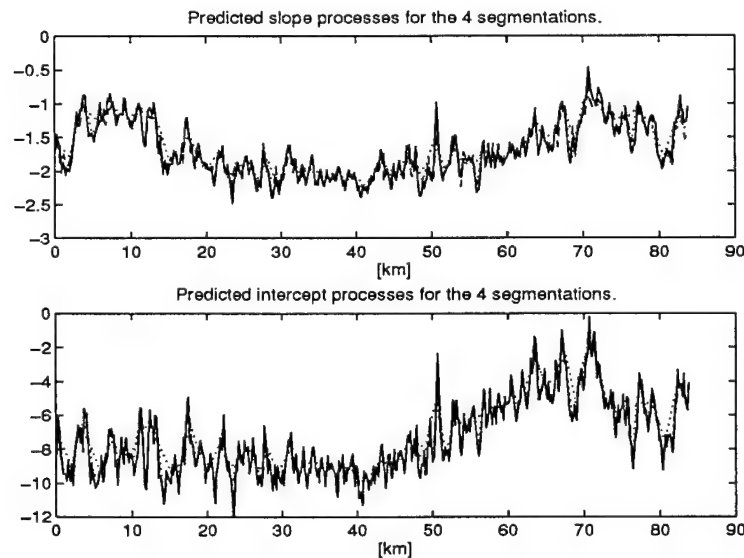


Figure 2.35: The filtered slope and log intercept processes obtained from Figure 2.33 as described in Section 2.3.3. This is comparable to Figure 2.14 and 2.24 insofar as segmentation effects have been removed. It is, however, another realization of the slope and log intercept processes with the correct statistical behavior.

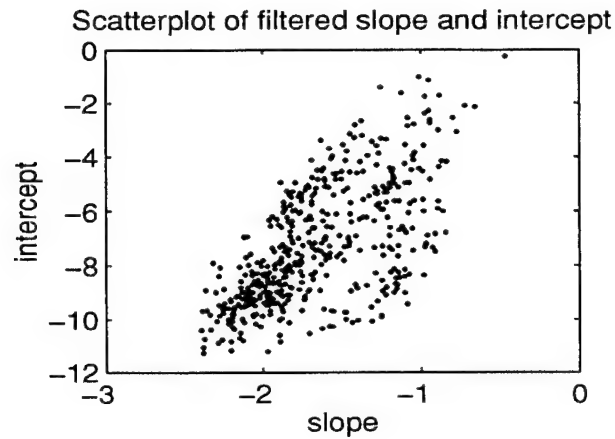


Figure 2.36: Scatterplot for the estimated slope and log intercept processes of Figure 2.35 (simulated data with random slope and intercept). This is like Figures 2.17 and 2.26. Note the positive correlation.

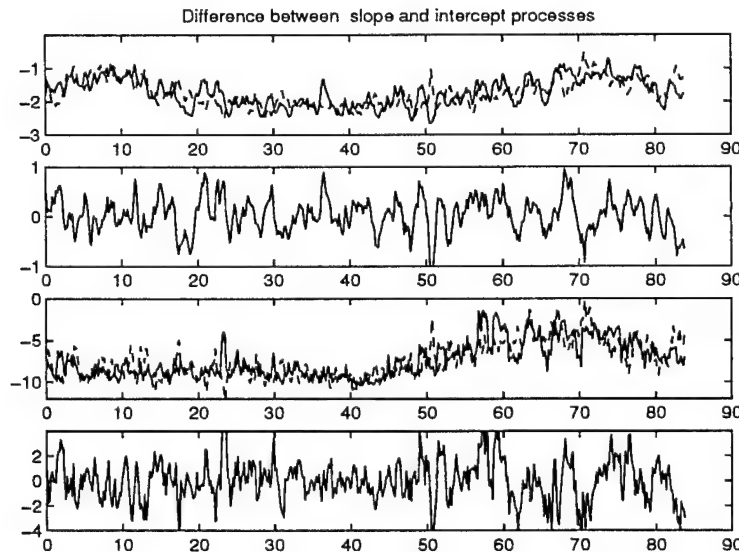


Figure 2.37: This is analogous to Figure 2.25 but now the slope and intercept for the actual data is compared to that obtained from the simulation with random slope and intercept as in Figure 2.36. The top frame shows two curves, the slope process for the actual data (Figure 2.14, top) and the slope process for the simulated data (Figure 2.36, top). The second figure from the top is the difference between these two curves. Note the size of the difference compared to that in Figure 2.25. The bottom two frames are the same as the top two but for the log intercept process.

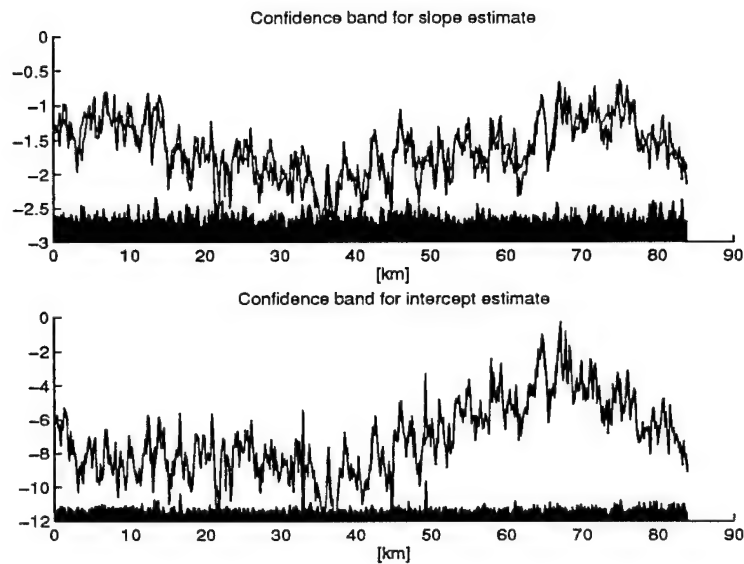


Figure 2.38: One realization of the estimated slope (top) and intercept (bottom) of the simulated temperature data with random slope and intercept. The shaded region at the bottom of each figure represents two standard deviations about the values used in the simulation, averaged over twenty realizations. This Figure should be compared to 2.27 where the same slope and intercept is used in all twenty realizations. The standard deviation is larger now. The two dashed curves in the top and bottom frame correspond to the slope and log intecept used in the simulation while the solid lines correspond to those estimated after the simulation.

## References

- [1] P. Abry, P. Goncalves and P. Flandrin, Wavelets, spectrum analysis and  $1/f$  processes, in 'Wavelets and Statistics', A. Antoniadis and G. Oppenheim editors, Springer Lecture Notes in Statistics 103, Springer 1995.
- [2] S. Mallat and Z. Zhang, Matching pursuit in a time-frequency dictionary, IEEE Trans. Signal Processing, 41, pp. 3397-3415, 1993.
- [3] H. Omre, K. Solna and H. Tjelmeland, Simulations of random functions on large lattices, in 'Geostatistics', A. Soares editor, pp. 179-199, Kluwer Academic Publishers, 1993.
- [4] B. Ripley, Spatial Statistics, Wiley, New York, 1981.
- [5] I. Karat and S. E. Shreve, Brownian Motion and Stochastic Calculus, Springer-Verlag, New York, 1991.

## A Simulation of power law processes

In this appendix we show how the realizations of the local power law model are being generated. We differentiate between the cases that the parameter sequence (log-intercept and slope of the power law) is given, and the case where we in a first step draw this from an appropriate stochastic model. With some abuse of terminology we refer to the first as deterministic simulation and the latter as random simulation. In the next sections we define the stochastic model for the local power law. Thereafter we outline the simulation algorithm.

The simulation algorithm corresponds to the one presented in [3]. In [3] our main objective was to define a simulation algorithm applicable for simulation a multiple dimensions. Here we only consider one-dimensional simulation, but use parameters that *vary* over the simulation interval, corresponding to a *local* power law. In the random simulation these parameters are realizations from appropriate stochastic models.

### A.1 Model of the process

Denote the stochastic process  $Y$  and a particular realization for  $y$ . We sample the process on a regular grid, the grid values are  $y_i$  for  $1 \leq i \leq 2^M \equiv N$ . The nodes we denote  $x_i = i \Delta x$ .

Let a Gaussian intrinsic power law process  $Y$  be defined by

$$E[(Y_{i+k} - Y_i)^2] = C|x_{i+k} - x_i|^p \quad (\text{A.1})$$

and by the requirement that the increments are zero mean Gaussian random variables. Hence, the marginal distribution of the samples need not be Gaussian. However, here we shall condition our realizations on  $y_0$ , hence the samples will be Gaussian and have bounded variance.

We next generalize (A.1) to a local power law, the model introduced in the paper. For a local power law process  $Y$

$$\begin{aligned} E[(Y_{i+k} - Y_i)^2] &= C(x_m)|x_{i+k} - x_i|^{p(x_m)} \\ x_m &= (x_{i+k} + x_i)/2. \end{aligned} \quad (\text{A.2})$$

It is from this model we want to draw realizations. As mentioned above the smooth parameter-sequences  $C(x)$  and  $p(x)$  are either defined a-priori, or they are draw from a stochastic model. We model the parameters as a truncated Gaussian exponentially correlated vector process. The stochastic model for the parameters,  $p$ , is defined by

$$\begin{aligned} E[(\tilde{p}(x_{i+k}) - \bar{p}(x_{i+k}))^T (\tilde{p}(x_i) - \bar{p}(x_i))] &= C \exp(-k\Delta x/a) \\ p &= \mathcal{F}(\tilde{p}) \end{aligned} \quad (\text{A.3})$$

with  $C$  being a covariance matrix and  $\mathcal{F}$  a truncation operator. For the truncation limits we used, set so as to ensure positivity, none values were truncated. Note that the ‘smooth-background’ or mean of the parameters vary with location, whereas the random residual is assumed to be stationary. Next we consider simulation from model (A.1). This will serve to motivate our approach for simulation from (A.2).



## A.2 Direct simulation of a stationary sequence

From (A.1) we can easily construct the covariance matrix of the sequence  $\{Y_0, \dots, Y_N\}$ , denote it  $C_y$ . Then, a sample from the process can simply be computed using the Cholesky factor  $G_y$  of  $C_y$  ( $C_y = G_y G_y^T$ ) by

$$y \leftarrow G_y \cdot \mathcal{N} + y_0 \quad (\text{A.4})$$

with  $\mathcal{N}$  being a vector of independent unit-variance Gaussian samples. This will in general be computationally too costly. We seek therefore an alternative simulation procedure, the procedure will be linear in the number of nodes. We simulate the process by a sequential simulation procedure.

## A.3 Sequential simulation of a stationary sequence

The simulation in (A.4) can be implemented as a sequential simulation in the following way. Simulate the samples  $y_1 \dots y_N$  in sequence, each sample being conditioned on the previously simulated samples. That is (using MATLAB-like notation)

```

y(0 : N) = 0;
for i = 1 : N
    y(i) = g(i, 1 : i - 1) * y(1 : i - 1) + g(i, i) * N(i);
endy = y + y_0;

```

with  $g(i, :)$  being the row vector containing the appropriate coefficients for the conditional simulation and  $N$  a vector of realizations of independent unit variance Gaussian random variables. With the right ordering in the simulation, the correlation with previous, distant samples might be small. In the markov case, each sample need only be conditioned on the previous sample, this one sort of 'screens' the effect of the previous values. If we let  $G_i$  denote the matrix that is the identity, apart from the  $i$ 'th row that is defined by  $g(i, 0 : i)$ , then

$$G_z = \prod_{i=1}^N G_i. \quad (\text{A.5})$$

We seek to construct the simulation sequence such that each sample need only be conditioned on a few previous samples, or such that  $g(i, 0 : i - 1)$  only has a few dominant terms.

Consider first a truncated version of a classical method for constructing Brownian motion, see for instance Section 2.3 [5]. This will show how to construct the right ordering such that we can condition on a small set of previous samples despite the fact that we are dealing with long-range processes.

```

% Classical method for constructing Brownian motion
function y = screen(M,dx,y0)
%
% Input
% M : dyadic dimension (#grid points is  $N = 2^M$ )
% dx : grid-spacing
% y0 : value of process at origin
% Output
% y : simulated process; column N-vector
%
N = 2^M;
ranN = randn(N + 1,1);
y(1) = y0;
 $\sigma = \sqrt{N \ dx}$ ;
y(N + 1) = y0 +  $\sigma \text{ ranN}(N + 1)$ ;
for i = 1 : M
    j = 2^(M-i);
     $\sigma = \sqrt{(dx \ j/4)}$ ;
    for k = 1 + j : 2*j : N + 1 - j
        y(k) = (y(k - j) + y(k + j))/2 +  $\sigma \text{ ranN}(k)$ ;
    end
end
y = y(2 : N + 1);

```

The simulation scheme starts out by initializing the boundary nodes. The algorithm then proceeds by drawing the samples on dyadic subgrids, creating a process of successively finer resolution. The main aspect of the procedure being that when the grid is refined, the new samples (one at each midpoint between samples at the previous level) need only be conditioned on the *two nearest neighbors*, both being simulated at the previous level. Thus, with this ordering in the simulation, the vector  $g_i$  contains only two non-zero entries.

Consider next simulation of fractional Brownian motion  $p \neq 1$ . Then  $g(i,0:i-1)$  will in general have more than two non-zero elements. However, sequential simulation with the same sequencing of nodes and the *same conditioning sets* as in the above construction gives accurate realizations also when we consider fractional Brownian motion. 'Accurate' in the sense of having essentially the right moments, see [3]. That is, we approximate the 'Cholesky factor'  $G_i$  with a factor having only two elements in its  $i$ 'th row, in addition to the diagonal element. Additional elements does not change the statistics by much. The diagonal element and the two off diagonal elements are chosen such that the sample has the right variance and expectation given the two neighbor elements. From symmetry the off diagonal coefficients equal 1/2. Hence the *only* change in *screen* is that the expressions for the conditional standard deviation  $\sigma$  is slightly changed and now depend on the values of  $p$  and  $C$ , see [4].

We next describe the specifics of the algorithm we used to draw realizations from the model A.2.

#### A.4 Screening simulation in non-stationary case.

Assume first that the parameter sequences are given. The parameter sequences characterize the log-intercept and the slope. These are the estimated slopes and log-intercepts for the finest resolution, segments of length  $2^p$ , for  $p=13$ . The total grid size is  $2^M$ , with  $M = 22$  in our case. The algorithm consists of two steps:

##### Step I

Define a 'super-grid' of size  $2^{(N-p)} + 1$  and draw the samples on this according to a model as in (A.2). The nodes in the super-grid corresponds to the boundary nodes for the segments of length  $2^p$  (defined as last node in each section). Within each section we have an estimate of the slope and the log-intercept. Note that the size of the supergrid is so small that we can actually use the decomposition (A.4). We chose to do the simulation on the supergrid sequentially. The value of a boundary node is drawn conditioned on the previous boundary node using the parameter values (log-intercept and slope) that corresponds to the section in between them.

##### Step II

In each section of the supergrid simulate a fractional Brownian motion by the screening algorithm. The simulation is conditioned on the two boundary nodes (in the supergrid).

Thus the function returning the simulated process is:

```
% Simulation of local power law
function y = SimLpl(M, dx, y0, logint, slope)
%
% Input
% M : dyadic dimension (#grid points is  $N = 2^M$ )
% dx : grid-spacing
% y0 : value of process at origin
% logint : the log-intercept parameter values; column vector
% slope : the slope parameter values; column vector
% Output
% y : simulated process; column N-vector
%
N = 2^M;
y = zeros(N, 1);
segments = length(slope);
k = N/segments;
p = log2(k);
for i = 1 : segments
    i1 = 1 + k (i - 1);
    i2 = k i;
    y(i1 : i2) = screen(p, dx, y0, logint(i), slope(i));
    y0 = y(i2);
end
```

The function *screen* is defined exactly as above only that the expressions for  $\sigma$  is slightly modified using the relevant values of *logint* and *slope*.

Finally, if we want to carry out a random simulation then the vectors *logint* and *slope* are sampled from the model (A.3). Simulation from this model is easily implemented since  $\tilde{p}$  is a Markov process.

## B Analysis of other aerothermal data sets

We repeated the scale spectral analysis of Part 2 for other data sets, the 97206-3 and 97206-15 (referred to as 03 and 15 in the captions). The results are quite similar and agree quite well with the analysis of Part 1, for the same data sets. The estimated slope and log intercept processes obtained by segmentation and filtering, and no averaging over adjacent blocks, is a bit choppier than what we find in Part 1 but the main features are quite comparable.

As we have already mentioned in the course of describing the analysis of the data in Part 2, the main overall consequence of the careful removal (minimization) of segmentation effects is that the estimated slope process shows more variability that appears to be intrinsic.